Journal of Volcanology and Geothermal Research 468 (2025) 108469

Contents lists available at ScienceDirect

Journal of Volcanology and Geothermal Research

journal homepage: www.journals.elsevier.com/journal-of-volcanology-and-geothermal-research

Transport and sedimentation of Pyroclastic Density Currents across topographic obstacles

Lucas Corna [a,b,*], Gert Lube [a], Daniel H. Uhle [a], Ermanno Brosch [a], Jim R. Jones [c], Michael Manga [d], Benjamin Andrews [e]

[a] School of Agriculture and Environment, Massey University, Palmerston North, New Zealand
[b] Istituto Nazionale di Geofisica e Vulcanologia, Sezione di Pisa, via C. Battisti 53, 56125 Pisa, Italy
[c] School of Food and Advanced Technology, Massey University, Palmerston North, New Zealand
[d] Department of Earth and Planetary Science, University of California, Berkeley, CA, USA
[e] Department of Mineral Sciences, Smithsonian Institution, Washington, DC, USA

ARTICLE INFO

Keywords:
Pyroclastic Density Currents
Gravity Currents
Large-scale experiments
Obstacle interactions
Topographic effects
Flow detachment
Spatiotemporal transport and deposition

ABSTRACT

Pyroclastic density currents (PDCs) can cross significant topographic obstacles. The processes that govern the interaction of PDCs with obstacles remain poorly understood leaving uncertainty in hazard planning and mitigation. Here, we report the results of large-scale experimental PDCs comprising hot volcanic particles and gas propagating across ridge-shaped obstacles. Observations from high-speed video and measurements of the velocity, density and temperature structure of the flows are used to identify the flow processes that occur when PDCs propagate across and become partially blocked by hill-shaped topographic obstacles; and how these characteristics are recorded in PDC deposits. The experiments show that the interaction of PDCs with ridges generate strong local perturbations to the internal flow velocity, density and temperature structure. These flow changes are linked to three main processes: the blocking of the lower, concentrated flow region in front of the obstacle; the compression and acceleration of the non-blocked flow regions on the stoss side; and the flow detachment behind the crest and formation of a turbulent wake before flow re-attachment downstream. Flow-topography interactions result in deposition and erosion rates that vary by three and two orders of magnitude, respectively, which explain the strong asymmetry of PDC deposits across topographic obstacles. The facies architecture of experimental deposits across ridges resembles those of natural PDC deposits from Te Maari and Taupō volcanoes (New Zealand). The findings of this study can guide the interpretation of PDC deposits or be taken into consideration in numerical models simulating the propagation of PDCs across complex topography for hazard forecast.

1. Introduction

Pyroclastic density currents (PDCs) are hot and mobile multiphase flows of volcanic particles and gas produced during volcanic eruptions (Druitt, 1998; Sulpizio et al., 2014; Lube et al., 2020).

PDCs are vertically density stratified with respect to particle volume concentration θ_V, which encompasses a wide range of *c.* $10^{-5} < \theta_V > 3 \times 10^{-1}$ inside a single flow (Lube et al., 2020). Three main regimes of particle-gas transport in PDCs can be distinguished based on the nature of particle-gas and particle-particle interactions that can occur across this spectrum of concentrations. In upper flow levels, well-coupled particle-gas motion as fully turbulent, fully dilute suspensions is associated with *c.* $\theta_V \lesssim 10^{-3}$. Strong particle-gas feedback across a wide range of turbulence intensity occurs at *c.* $10^{-3} \lesssim \theta_V \lesssim 3 \times 10^{-1}$. This characterises a recently identified, intermediate regime (Breard et al., 2016) that is associated with increased particle clustering and sedimentation (Breard and Lube, 2017; Lube et al., 2020; Brosch et al., 2022). With downward increasing particle concentration, the intermediate regime transitions into a weakly turbulent to non-turbulent basal flow region of high particle concentration of *c.* $\theta_V \gtrsim 3 \times 10^{-1}$. Here, particle stresses dominate over hydrodynamic stresses and particle-gas transport may occur in a thin bedload layer or a thicker underflow region of dry granular (Lube et al., 2007) to gas pore-pressure-modified granular flow (Roche, 2012). Historically, researchers have tried to

* Corresponding author at: School of Agriculture and Environment, Massey University, Palmerston North, New Zealand.
E-mail address: lucas.corna@ingv.it (L. Corna).

https://doi.org/10.1016/j.jvolgeores.2025.108469
Received 2 July 2025; Received in revised form 2 October 2025; Accepted 8 October 2025
Available online 10 October 2025

distinguish two broad types of PDC deposits as endmembers of either dominantly dilute or concentrated PDC transport. Conceptual models for concentrated PDCs, also termed pyroclastic flows, envisage a granular-fluid, valley-ponding underflow that is overlain by a turbulent dilute ash-cloud surge region. In analogy to powder snow avalanches and dilute turbidity currents, models for dilute PDC endmembers (also pyroclastic surges and blasts) conceptualise a fully turbulent particle-laden gravity current above a thin bedload region.

An intriguing characteristic of concentrated and dilute PDCs is their variable ability to surmount and propagate across significant topographic obstacles. This behavior can lead to PDCs taking unexpected flow paths and engulfing potentially densely populated or cultivated areas behind obstacles that may not have been previously considered in hazard planning. Examples of the risk associated with such PDC behavior include the burial of the Roman city of Herculaneum in 79 CE (e.g. Gurioli et al., 2002), the lateral blasts of Mount *St*. Helens in 1980 (e.g. Moore and Rice, 1984), or the destruction of the community of San Miguel Los Lotes near Fuego Volcano in Guatemala in 2018 (Risica et al., 2022; Charbonnier et al., 2023). During the lethal 26 October 2010 eruption of Gunung Merapi (Indonesia), PDCs crossed a total of four high and steep-sided ridges and destroyed the village of Kinahrejo. The villagers of the touristic village of Kali Urang only narrowly escaped the same fate when the PDCs became locally blocked by a fifth ridge (Cronin et al., 2013; Komorowski et al., 2013). During the 2012 eruption of Te Maari (New Zealand), mobile low-volume blast-like PDCs advanced over a series of five ridges to engulf the country's most frequented hiking track and a tourist hut before becoming blocked by a sixth ridge (Lube et al., 2014; Breard et al., 2015). Understanding how PDCs interact with topographic obstacles is thus an important prerequisite to inform hazard modelling approaches and risk mitigation strategies.

Several field studies have addressed this problem through analyses of the characteristics of PDC deposits emplaced across topographic obstacles (e.g. Wilson, 1985; Fisher, 1990; Dade and Huppert, 1996; Bursik et al., 1998; Burgisser, 2005; Sulpizio et al., 2008; Cas et al., 2011; Brand et al., 2016). These studies reported strong variation in sedimentary facies and thickness of deposits across obstacles. For instance, in proximal deposits of large ignimbrites, massive, poorly sorted, thick deposits on the obstacle stoss side transition into thinner, stratified deposits on the crest and alternating coarse-rich and fines-rich lenses of PDC deposit on the lee side (Wilson, 1985; Sulpizio et al., 2008). Multiple mechanisms were proposed to explain the ability of PDCs to surmount topographic obstacles, such as a sufficiently high flow momentum (Wilson, 1985), dilute flows crossing topography when thicknesses exceeded the height of the terrain (Dade and Huppert, 1996; Fisher et al., 1993), rapid suspension sedimentation in blast-like PDCs (Breard et al., 2015), valley filling and consecutive flow avulsion (Lube et al., 2011; Risica et al., 2022), flow compression and acceleration due to momentum balance as basal particles accumulate on the slope (Freundt and Schmincke, 1985), or sediment trapping and rapid topography modification during flow emplacement (Brown and Branney, 2013).

On the lee side of obstacles, the layered characteristics of the deposits of PDCs have been interpreted as the flow adhering to and following topography (e.g. Druitt, 1998; Branney and Kokelaar, 2002). On the other hand, through a reconnaissance mapping of the blast deposits and tree damage of the 1980 eruption of Mount *St*. Helens, Gardner et al. (2018) proposed a process for (dilute) PDCs jumping from the crest and re-attaching on the leeside of ridges. They modelled this process as a combination of ballistic flight and downward expansion due to entrainment of ambient air into the basal, 'jumping' flow.

Experimental analogue models have also been used to explain PDC dynamics. Laboratory experiments of aqueous gravity currents that simulated the interaction of PDCs with obstacles reported the formation of hydraulic jumps, backflows on the lee side and upstream-migrating bores on the stoss side of obstacles (e.g Alexander and Morris, 1994; Woods et al., 1998; Wilson et al., 2018). Woods et al. (1998) and Oshaghi et al. (2013) noted the hydraulic control of obstacles on density currents with, for example, subcritical currents becoming supercritical upon crossing an obstacle, before potentially transitioning back to subcritical flow in agreement with the theory of Hunt et al. (1978). On the other hand, experiments on granular flows revealed that they were following ballistic trajectories, also controlled by a relation between the flow thickness and the obstacle height (Hákonardóttir et al., 2003). In general, our understanding of the interactions of constant density, continuous flows as well as of (weakly compressible) turbidity currents with wall-mounted obstacles are more mature than for PDCs. Multiple experimental and numerical studies have highlighted the existence of horseshoe vortices, flow separation and vortex shedding in these constant-density and continuous flow situations (e.g. Baker, 1979; Mason and Sykes, 1979; Mason and Morton, 1987; Belcher and Hunt, 1998; Nasr-Azadani and Meiburg, 2014).

The scaling properties of aqueous gravity currents and simple continuous flows strongly differ from PDCs (Burgisser et al., 2005), indicating a need for more accurate experimental models, notably through large-scale experiments of particle-laden gas flows. For instance, Andrews and Manga (2011) introduced a large-scale experimental device to simulate the interaction of PDC analogues of hot talcum powder and air with wall-shaped barriers. They demonstrated that such barriers could induce the lift-off of co-ignimbrite plumes affecting PDC runout. The low turbulence intensity, as well as the limited ranges in particle-size and particle volume concentration in these experiments, however, meant that only the fully dilute turbulent endmember of the broad spectrum of PDC flow regimes and particle-gas transport could be investigated. In nature however, PDCs range from fully dilute particle-fluid gas to fully granular interactions.

The present study is motivated by the paucity of direct observations and measurements of internal processes of particle-gas multiphase flow during interactions of PDCs with obstacles. To this end, we report the results from a series of large-scale experiments of PDC analogues of hot natural volcanic material and gas, composed of a basal underflow and an overriding ashcloud surge, propagating across ridge-shaped, wall-mounted obstacles.

We present observations from high-speed cinematography and direct measurements of the internal velocity, density and temperature structure of the flows. This information is used to interrogate what types of flow processes occur when PDCs flow across and become partially blocked by hill-shaped topographic obstacles, how these processes modify the PDC flow structure, and how they are recorded in the spatiotemporal deposit architecture.

2. Methods

2.1. PELE set-up and scaling

The Pyroclastic flow Eruption Large-scale Experiment (PELE, Fig. 1a) is an experimental facility designed to synthesize and study the transport and depositional mechanisms of PDCs at conditions that are dynamically and kinematically scaled to natural PDCs. Detailed descriptions of the experimental design and protocol are given in Lube et al. (2015) and Uhle et al. (2024). At PELE, experimental PDCs are generated by the controlled gravitational collapse of a suspension of hot volcanic particles and air from an elevated hopper into an instrumented runout section. The set-up is comprised of four main elements (Fig. 1a): (i) Tower: a 13 m-high structure with an elevator system that drives a 0.7 m^3 hopper, including an internal heating system, to target height. The heating process is measured by thermocouples, and the hopper is connected onto four load cells to measure the time-variant mass discharge.; (ii) Column: a $\leq$9 m high shroud of heat-resistant cloth through which the discharged mixture falls under gravity; (iii) Chute. A 14.2 m long and 0.5 m wide multi-instrumented channel section with 0.6–1.8 m high sides of tempered glass. The first 11.7 m were inclined at 6° while the last 2.5 m of the channel was horizontal; and (iv) Outflow. A 16 m-long flat instrumented and unconfined runout section.

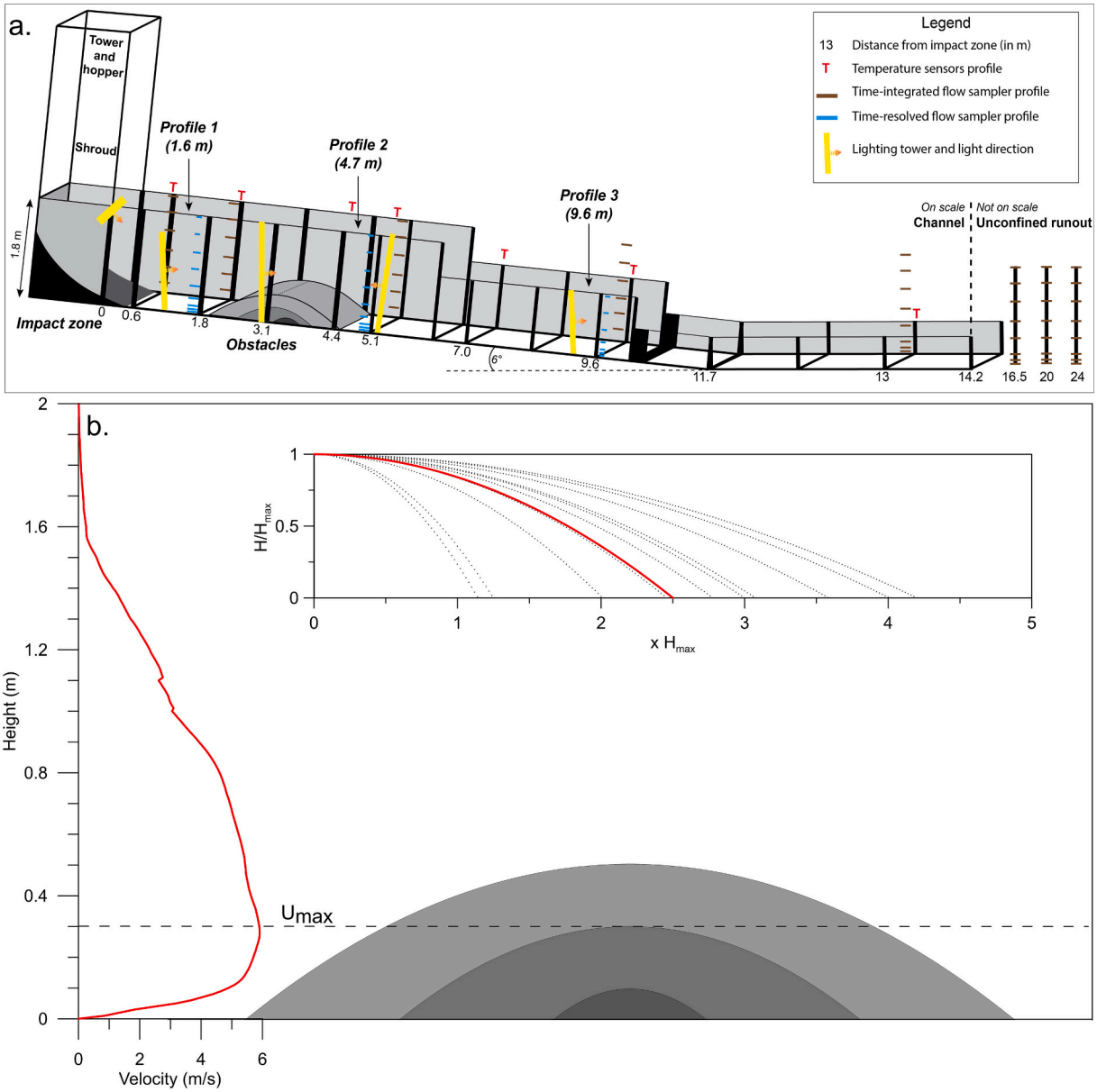

Fig. 1. Experimental setup. (a) Sketch of the PELE setup indicating the position of the three obstacles and the three main profiles labelled 1 to 3. (b) Comparison between the heights and shapes of the three different obstacles and the typical time-average velocity profile at position Profile 1 in a PELE experiment. Obstacles are scaled to be lower, higher or similar height than the height of the maximum velocity *Umax*. In the inset, the natural obstacles are plotted using Eq. 3 in dotted curves and scaled to the same height. The red curve shows the average value used in the experiments. (For interpretation of the references to colour in this figure legend, the reader is referred to the web version of this article.)

The experimental flows constitute multiphase flows of natural, heated pyroclastic material and air. To quantify the scaling similarity of natural PDCs and our experimental analogues, characteristic fluid mechanic and thermodynamic non-dimensional numbers are listed in Table 1. This table demonstrates the partial overlap in scaling parameters and dynamic relevance of experimental PDCs with real-world flows.

For each of the three experiments described here, we used 200 kg of an ash-rich facies of the 232 CE Taupō ignimbrite that we collected c. 17 km northeast of the inferred vent (Wilson, 1985) and screened to particle diameters <16 mm. This polymodal mixture (grainsize and particle density distributions are shown in Supplementary material 1), with main components of highly vesicular and sub-rounded pumice, angular glass shards, free crystals and sub-ordinate lithic particles, contains particle sizes from 2 mm to 16 mm (9 to −4 Φ), a median particle diameter of 422 μm (1.2 Φ) and a sorting coefficient of 93 μm (3.2 Φ). It contains c. 26.5 wt% of extremely fine ash (particle diameter < 63 μm) and c. 27.5 wt% of lapilli clasts (> 2 mm). Under the experimental flow conditions, this grain-size range reproduces the full spectrum of gas-particle coupling regimes of natural PDCs (i.e., Stokes number $St <<1$, $St \sim 1$ and $St>> 1$). The static friction coefficient of the mixture equals 0.8, while the wall friction coefficient is 0.85. Here and in the following, the grainsize terminology of White and Houghton (2006) is used, while standard sedimentological terms are used to describe thicknesses of deposit layers (e.g., beds and lamina). Previous experiments (e.g. Brosch and Lube, 2020) used a blend of two facies of Taupo ignimbrite deposits with c. 20 wt% of extremely fine ash resulting in an approximately Gaussian grainsize distribution. In this study, and to enable the development of a mobile underflow at the base of experimental PDCs, a single polymodal deposit with a larger proportion of extremely fine ash was deployed. After field collection, the material was dried in an oven at 100 °C for one week and stored.

For the experiments, the pre-dried mixture was transferred into the

Table 1
Table of non-dimensional numbers of the experiments of this study and natural PDCs. Natural data extracted from Burgisser et al. (2005), Choux and Druitt (2002), and Roche (2012).

Scaling parameters	*Symbol*	*Unit*	*PELE experiments with obstacles*	*Natural dense PDCs*	*Natural dilute PDCs*
Particle size	*d*	mm	0.002–16	0.002–1000	0.002–1000
Velocity	*U*	m s^{-1}	3–12	5–30	10–200
Density	ρ	kg/ m^3	1–200	10–500	1–100
Reynolds	*Re*	–	10^5–10^7	–	10^6–10^9
Richardson	Ri	–	0.5–5	10^{-4} - 10^1	0–10
Densimetric Froude	*Fr'*	–	0.6–15	1–10	~ 1
Stokes	S_T	–	10^{-3} - 10^1	–	10^{-3} - 10^7
Stability	Σ_T	–	10^{-2} - 10^1	–	10^{-6} - 10^9
Rouse	Pn	–	1–20	–	10^{-3} - 10^2
Bagnold	Ba	–	10^0–10^2	10^{-2} - 10^2	–
Darcy	*Da*	–	10^0–10^3	10^2–10^4	–
Savage	Sa	–	10^{-6} – 10^{-5}	10^{-9}–10^{-6}	–

hopper suspended 7 m above the channel. The mixture was heated at 120 °C for three days to remove residual moisture that could have intruded during storage and might produce cohesion among the small size fraction of particles. The hopper trap doors were opened with an electric trigger signal that also provided synchronization for sensors and cameras to record the flow. A layer of 4–8 mm subrounded greywacke pebbles was glued to the base of the channel. For natural PDCs with 100–500 m thicknesses, this condition represents geometrically scaled roughness of 0.2–2.2 m. This is based on geometric scaling for 100–500 m thick natural PDCs as

$$R = r\frac{H_{PELE}}{H_{PDC}} \quad (1)$$

with R the scaled roughness, r the deployed roughness, H_{PELE} flow thickness in experiments, and the natural flow thickness H_{PDC} of 100–500 m.

The overall evolving flow shape was recorded with eight cameras at 30 to 120 frames per second.

Four high-resolution, high-speed cameras recorded the passage of the flow at 1000 frames per seconds at selected locations (Fig. 1a, Supplementary material 2). Two-dimensional velocity fields were measured from the videos through Particle Image Velocimetry (PIV) using the software PIVlab (Thielicke and Stamhuis, 2014).

Additional high-resolution cameras recorded close-ups of the aggrading deposits at different locations along the channel. These were set to sufficiently long shutter speeds to map the evolving boundary of static (deposited) and blurred (moving) particles at sub-millimetric resolution. Grain-size distributions of deposits, which were collected as either bulk samples or as time-resolved layer by layer samples, were determined by a combination of wet-sieving and Laser-Particle-Sizing.

At flow distances of 1.6 and 4.7 m from impact, vertical arrays of transparent sediment samplers collected the flowing mixture at heights *z* of 3.5, 8, 15, 25, 45, 75, 110, 145 and 180 cm above the channel base. During the experiment, the sequential filling the flow samplers was filmed with highspeed cameras. These samplers are open on the upstream side allowing the flow to enter through the 1.96–4 cm^2 cross-sectional area while on the downstream side, a multilayered 16 μm mesh allows only the gas-phase of the flow to exit, leading to accumulation of the transported particles inside the sampler. From this we measure continuous data of flow sediment passing a position as a function of time. Downslope velocity components *u(t)* of the flow at a position 5 cm upstream of each flow sampler were obtained through PIV. The weight and density of the material deposited inside the flow samplers was measured at selected time intervals to calculate the time-variant porosity of the captured sediment, as well as the sediment grain-size distribution. Using the method of Brosch and Lube (2020), particle solids-concentration C_S can be computed as:

$$C_s(z,t) \text{ with } C_s(z,t) = \frac{V_d(1-\varepsilon)}{UA_0t} \quad (2)$$

with V_d the volume of sediments accumulated in the sampler, ε the sediment porosity, U the flow velocity, A_0 the tube opening area and t the selected time interval. The flow density ρ_f was then calculated with $\rho_f = \rho_s C_s + \rho_a(1 - C_s)$, with ρ_s the particle density and ρ_a the air density. Uhle et al. (2024) recently confirmed the accuracy of the density measurement method through independent, highly time-resolved measurements of flow velocity and dynamic pressure through the Bernoulli relationship.

At flow distances of 0.6, 1.8, 4.0, 4.7, 7.0, 9.6 and 13 m from impact, time series of flow temperature were measured in vertical profiles via bare-wire, fast-response thermocouples that sampled at 70 Hz at heights of 3.5, 11, 21, 45, 75, 110, 145 and 180 cm above the flow base (Supplementary material 2).

2.2. Obstacle design, scaling and position

Natural hills and ridges in PDC pathways come in a range of shapes and sizes. Due to the complexity of the large-scale experiments and associated data analysis, a series of three experiments for the situation of partial flow blocking by ridge-shaped obstacles perpendicular to the flow direction was designed. In these experiments, the shape of the hill model was kept constant, while its size was varied (Fig. 1b) from 0.1 m to 0.5 m high, compared with a c. 1–1.5 m thick experimental PDC with velocity maxima typically at heights of about 0.3 m.

Using 10–20 m resolution Digital-Elevation models of Mount Saint Helens (USA), Tongariro (New-Zealand), Bandai (Japan) and Merapi (Indonesia) volcanoes, the shapes of prominent ridges of various dimensions around these volcanoes were analysed. This showed that, on average, the aspect ratio H_{crest}/L_{max} of the hills is 0.2, with H_{crest} the height of the obstacle at the crest and L_{max} the total length of the obstacle. In other words, obstacle lengths are five times the obstacle heights (inset in Fig. 1b).

The hill or ridge shape is well represented by a parabolic demi-shape geometrically defined as:

$$H = H_{crest} - \left[\frac{H_{crest}}{(L_{max}/2)^2}\right] * L^2. \quad (3)$$

with H the height of the obstacle at a distance L from the crest. Three hill models of different sizes were built with H_{crest} of 0.1 m, 0.3 m and 0.5 m (associated with lengths L_{max} of 0.5, 1.5 and 2.5 m, respectively). These heights were selected to obtain obstacles smaller, of similar size, or larger than the average height of *c.* 0.3 m of the velocity maximum (H_{Umax}) of the experimental PDCs (Fig. 1b). The crest of the ridge-shaped obstacles were positioned into the instrumented flow channel at a distance of 3.3 m from the impact zone.

To compare the vertical velocity, density and flow grain-size structure of the experimental PDCs before and after the obstacle, a first vertical sensor profile was installed before the obstacle at a runout distance of 1.6 m, which we call the *Profile 1*, and another one was placed behind the obstacle at 4.7 m, which we refer to as the *Profile 2* (Fig. 1a).

For simplification in this article, experiments are named experiments S, M and L (referring to Small, Medium and Large obstacles).

3. Results

3.1. General flow characteristics

The experimental PDCs propagate to *c.* 30 m from the impact zone,

where they strongly decelerate and finally become positively buoyant and lift off. The characteristic time of flow passage at a static observer location along the flow runout is approximately eight seconds, comparable with the duration of discharge from the hopper. The flow duration lasts approximately 20 s, and most of the deposition occurs in the first seconds after flow arrival, but the deposition of fine ash from the phoenix cloud can take several minutes. The flow structure of the experimental PDCs, at Profiles 1 and 2, was characterised through height-time plots (i.e., kymographs) of high-speed videos (Fig. 2), and through timeseries measurements of flow velocities, densities (Figs. 2 and 3) and temperatures (Supplementary material 3) in vertical profiles.

Flow structure before the obstacle. At Profile 1, the density current structure is fully developed. Fig. 2a depicts the streamwise structure, which is comprised of a leading, *c.* 1.5 m thick head, a *c.* 1.1 m-thick density current body region and a density current tail region. Turbulent eddies shedding from the head vortex feed an ash cloud above the body and to heights of *c.* 1.5–2.1 m above the base. Due to vigorous entrainment of ambient air, the head is more dilute than the trailing body (graph of depth-averaged flow density for experiment M shown in Fig. 2). Behind the head, sedimentation leads to the development of a dense bedload region, which grows in thickness over time, and, from c. 3 s after flow arrival, transitions into a dense, up to *c.* 0.1 m-thick, granular-fluid underflow. The total time- and height-averaged flow density has a value of *c.* 6.5 kg m^{-3} corresponding to a density ratio with the ambient air of around five. The time- and height-averaged density of only the dilute part of the experimental PDCs (that is the flow above the dense underflow) is *c.* 3.5 kg m^{-3}, corresponding to a density ratio of around three.

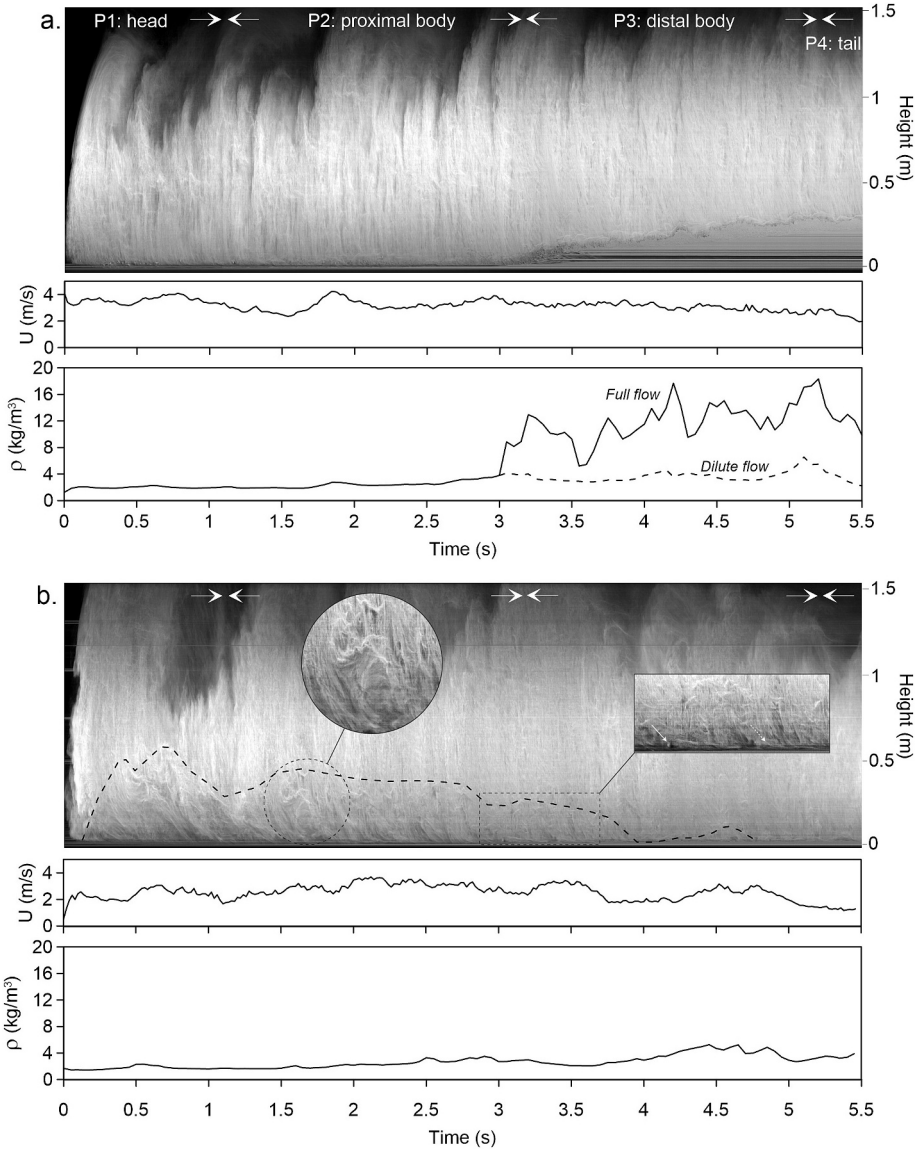

Fig. 2. Kymographs showing the structure of the evolving flow for Experiment M at Profiles 1 and 2. Time series of depth-averaged velocity and density are shown below each kymograph. White arrows at the top delineate the different flow phases P1–P4 associated with the density current head, proximal body, distal body, and tail regions (see section 3.2.) (a) At Profile 1, the density current is composed of a dilute turbulent head and proximal body regions that overlay a c. 1–3 cm thick bedload. After c. 3 s, the centimetric bedload region transitions into a decimetric, granular-fluid underflow, and flow density increases. The dashed curve in the density time-series corresponds to the depth-averaged density of only the dilute part of the flow, excluding the dense underflow. (b) At Profile 2, the dilute, turbulent head, body and tail regions remain distinct. The density current is devoid of a dense underflow. The black dashed line marks the upper boundary of an up to c. 0.6 m-thick visibly disturbed, vortical lower flow region, where no bedload is present, and which corresponds to the turbulent wake that forms behind the ridge crest. Insets highlight the disturbed flow structure in the wake and later, the intermittent bedload formation and saltating lapilli at the base. The flow density is lower than at Profile 1 as shown in the time-series.

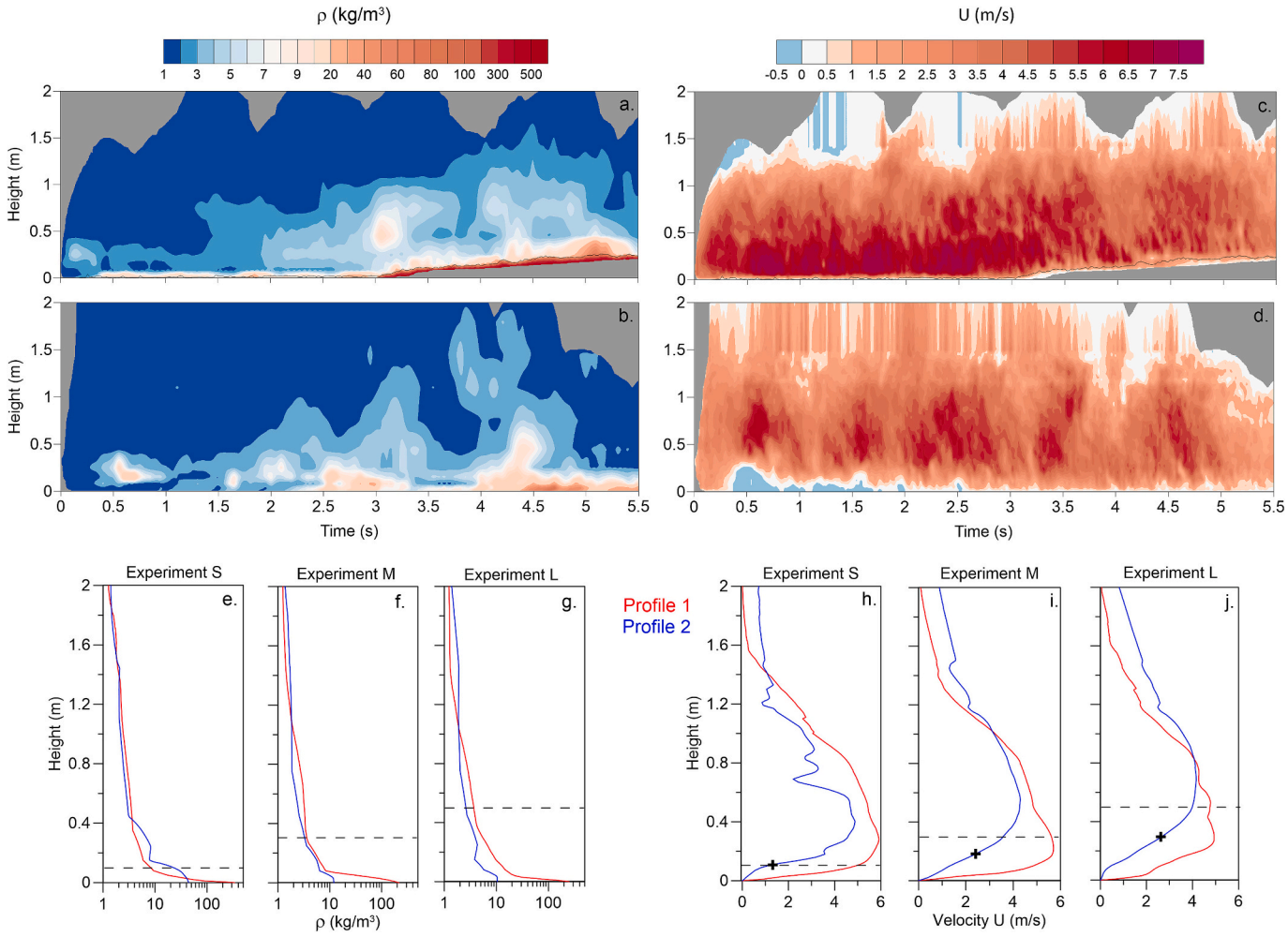

Fig. 3. Density and velocity structure of the experimental flows. (a-b) Height-time contour plots of flow density for (a) Profile 1 and (b) Profile 2 of Experiment M. The grey area at the base shows the building of deposits and the solid black line marks the height of the bedload region. (c-d) Height-time contour plots of downstream velocity component (U) for Profile 1 (c) and Profile 2 (d) for Experiment M. Note the negative velocities in the wake marked with blue colors indicating backflow. (e-g) Time-averaged vertical profiles of flow density for experiments S, M and L at Profiles 1 and 2. The dashed lines refer to the height of the obstacle for each experiment. The height on the vertical axis corresponds to the height above the deposits. (h-j) Time-averaged vertical profiles of flow velocity for experiments S, M and L at Profiles 1 and 2. The plus sign marks the position of an inflection point in the velocity profiles below which profile have a low shear, convex profile, and above which profiles have a concave shape. The dashed lines refer to the height of the obstacle for each experiment. The height on the vertical axis corresponds to the height above the deposits. (For interpretation of the references to colour in this figure legend, the reader is referred to the web version of this article.)

Fig. 3a depicts the height- and time-varying flow density structure at Profile 1 for experiment M, while time-averaged profiles of the vertical flow density structure for all three experiments are graphed in Fig. 3 e–g. Due to the same starting conditions, the three experiments show similar time-averaged vertical density profiles, which highlight the strong density stratification of the bi-partite experimental PDC (i.e., PDC composed of basal underflow and overriding ash-cloud).

The vertical velocity structure is characterised by strong shear of the dilute, turbulent flow with the lower flow boundary (or slower moving underflow) and weaker free shear with the ambient air above (Fig. 3c). The height of the velocity maximum at c. 0.3 m, separates the lower wall-region from an upper jet-region. Time-averaged profiles of the vertical velocity structure for the three experiments are shown in Fig. 3h–j.

Flow structure after the obstacle. Fig. 2b illustrates the time- and height-varying flow structure at Profile 2, which is situated three metres downstream of Profile 1, in a kymograph using the example of experiment M. In comparison to Profile 1, the flow thickness, particularly in the head and frontal body flow regions, has increased (up to *c.* 3.5 m), but the general density current structure of head, body and tail regions remains clearly visible. Importantly, there is no PDC underflow, which, in all three experiments, becomes entirely blocked by and deposits on the stoss side of the ridge. Because of the blocking of the lower flow region, in comparison to Profile 1, the time- and depth-averaged flow density is strongly reduced, by *c.* 20 % for experiment S, and by *c.* 60 % for experiments M and L. The depth-averaged density of only the dilute flow region (i.e., any part of the flow above dense bedload and/or underflow regions) has only decreased slightly and is correlated to the increase in flow thickness after the obstacle (depth-averaged density timeseries in Figs. 2 a and b). The disturbance of the vertical density stratification by the obstacles becomes more enhanced with increasing hill size (c.f., Figs. 3e, f and g).

The kymograph at Profile 2 (Fig. 2b), and up to around 4.7 s after flow arrival, highlights a lower, up to c. 0.6 m thick flow region (delineated by a black dashed line) that is markedly disturbed (note vortical flow structure in enlarged circular inset in Fig. 2b). During this part of the flow passage, the experimental PDC has not developed a bedload region. The intermittent development of a bedload as saltating pumice lapilli (solid white arrow) and/or dense granular flow (dashed white arrow) occurs at around 3 s (note enlarged rectangular inset in Fig. 2b).

The disturbed vortical lower flow region is distinct in height-time

contour plots of the downstream velocity component (Fig. 3d). In comparison to Profile 1, this region is characterised by markedly lower and, particularly in the lower flow region, temporary negative (i.e., upstream directed) velocities. The disturbance of the vertical velocity structure of the experimental PDCs behind the obstacle is also clearly visible in time-averaged vertical velocity profiles for all three obstacle heights (Figs. 3 h–j). These vertical profiles have a distinct inflection point (marked by a plus symbol), below which the vertical profile has a convex shape, and above which the velocity profile is characterised by a concave form typical for logarithmic boundary layers in turbulent flow (e.g. wall region in Profile 1). With increasing obstacle size, the absolute height of the inflection point increases, while, relative to the height of the obstacle, the inflection point moves systematically downward. In comparison to Profile 1, the height of the velocity maximum increases with increasing obstacle height.

The disturbed vortical lower flow region also has distinct thermal characteristics (Supplementary material 3). Upstream of the obstacle, the flow has high and downwards-increasing temperature because of downward-increasing particle concentration, associated with a dense flow in bedload and/or underflow regions. After the crest, in comparison to the flow region above, the disturbed region is characterised by initially colder and approximately ambient (air) temperatures. Over time, temperature increases in this region except for the lower approximately 0.1 m. The onset of higher temperatures in this lower flow region at Profile 2, coincides with the disappearance of the disturbed lower flow and the re-establishment of a bedload region at the base of flow at around 4.7 s.

Associated with the marked changes of the vertical flow structure (i.e., thickness, density, velocity and temperature) before and after the obstacles, are systematic changes of the densimetric Froude number *Fr'*, which is the ratio of inertial and gravitational forces defined as:

$$\mathrm{Fr}' = \frac{U_c}{\sqrt{\frac{\Delta\rho}{\rho_c} g h \cos\theta}}. \quad (4)$$

with U_C the flow velocity, $\Delta\rho$ the density difference between flow and atmosphere, ρ_C the flow density, g the acceleration of gravity, h the flow thickness and θ the channel slope angle. Timeseries of *Fr'* were calculated for both Profiles 1 and 2 for the three experiments considering only the volumetrically dominant, turbulent ash-cloud surge flow region that precedes and overrides the concentrated basal underflow region (Fig. 4). Through this definition of the Froude number for the particle-laden density current sensu stricto, the measured values are directly comparable with those obtained for other types of experimental and natural density currents.

At P1, the density current head regions in experiments S, M and L are characterised by similar, critical to mildly supercritical values of the Froude number of c. $1.2 \lesssim Fr' \lesssim 1.4$. The highest values of *Fr'* in the first c. 0.5 s of flow are associated with a strongly increasing flow thickness during initial passage of the front of the density current head region. During the passage of PDC body regions, the three experiments show systematic differences in the time-variant evolution of *Fr'*. In experiment S, *Fr'* remains approximately constant with a time-averaged value of $Fr' \sim 1$. In experiment M, and even more pronounced in experiment L, the Froude number decreases with time to values of c. 0.6 and 0.4 for experiments M and L, respectively.

The difference in Froude numbers in the three experiments, despite the identical starting conditions, is rooted in a flow perturbation created through the partial blocking of the ash-cloud surge flow region during interaction with the ridge. This perturbation propagates upstream and is associated with an increase in flow depth and a resulting reduction in *Fr'*. The upstream-propagating, partial blocking effect increases with increasing obstacle height as a larger fraction of the flow depth becomes perturbed. A secondary effect is created through the variable lengths and upstream starting locations of the three ridges, while the position of their crests is identical. This condition means that, with increasing obstacle size, any flow perturbation due to partial blocking is propagated earlier upstream in experiments with larger obstacles. Consequently, the three experiments show different time-variant changes of *Fr'*.

After the obstacles, at P2, as the flow thickness increases, the Froude numbers in all three experiments are sub-critical and take markedly similar time-averaged values between c. 0.7 and 0.8, while fluctuations in *Fr'* are less pronounced than at P1. These observations are in agreement with the known hydraulic control of wall-mounted obstacles onto variably Froude-critical density currents (e.g. Hunt et al., 1978; Woods et al., 1998; Nasr-Azadani and Meiburg, 2014).

3.2. PDC propagation over obstacles

To understand the perturbation of the vertical flow structure due to interaction with hill-shaped obstacles, we analysed high-speed videos of the experimental PDCs with Particle-Image-Velocimetry (PIV). The PIV captured either the entire hill (for the small obstacle) or the lee side of the hills including their crests (for the intermediate and large obstacles). From the PIV data, downslope (U) and vertical (V) components of velocity and flow streamlines were computed. In the following, we describe and subdivide the processes of PDC-obstacle interaction in four characteristic but highly transient flow phases. These four phases, which are recognised in all three experiments, correspond approximately to the passage of the head, frontal body, distal body, and tail regions of the experimental PDCs over the obstacle.

3.2.1. Phase 1

During propagation of the gravity current head region across the obstacle, the relatively dilute incoming flow, with depth-averaged densities of c. 1.85–2.06 kg m^{-3}, is entirely non-depositional. At the base of the current, a < 0.01 m-thick bedload layer of rolling and saltating particles develops, but there is no dense underflow.

On the stoss side, flow streamlines of the impacting lower part of the

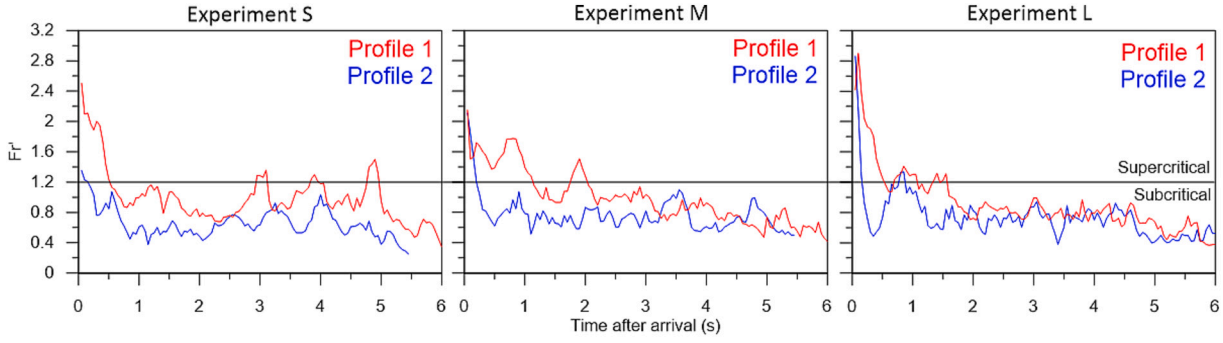

Fig. 4. Time series of the densimetric Froude number *Fr'* for the three experiments at Profiles 1 and 2. The black line at *Fr'* = 1.2 separates supercritical and subcritical regimes. The first c. 0.5 s of flow are associated with high *Fr'* values due to strongly increasing flow thickness during initial passage of the front.

current strongly converge (Fig. 5a and e). This convergence is associated with a strong local acceleration that affects the flow up to approximately the height of the obstacle crest. As the head climbs the stoss side, the basal part of the flow is advected upward and deflects the upper part of the current. This leads to a local backward rotation of the upper flow regions, which is particularly prominent in the cases of the intermediate and large obstacles.

Immediately downstream from the hill crest, flow streamlines strongly diverge in the adverse pressure field (Fig. 5d and h). This leads to the separation of the turbulent flow boundary layer and detachment of the flow. The detachment angle θ, defined as the angle between the channel slope and point of detachment ($\theta = 90°$ corresponding to the crest), increases during Phase 1 to values up to c. 130° (Fig. 9b). Before re-attaching at a downslope distance from the crest D_R, the separated flow encloses an initially cold volume of ambient air. Strong shear of the basal, separated flow within this volume enables a spot of turbulence to develop on the upper lee side (Fig. 5a-d). Over time, and accompanied with sediment entering it, this spot grows into a large rotating vortex that propagates downslope creating a turbulent wake (Fig. 5e-h). The wake is characterised by slow and temporarily reversed flow (note negative downstream velocity components U in Fig. 5c and g) and coincides with the disturbed vortical flow region.

3.2.2. Phase 2

The passage of the frontal body region is associated with an increase in flow density to c. 3.6–7.8 kg m^{-3} (Figs. 2 and 3). The thickness of the bedload layer generally increases up to a few centimetres and comprises stages of transport of rolling and saltation alternating with times of mobile, dense, granular avalanches that start climbing the stoss side. Overall, the experimental PDCs remain mostly non-depositional, although thin deposits are gradually emplaced on the stoss side of the hills.

On the stoss side, the converging and accelerating flow is associated with a strong compression of the dense basal gas-particle mixture. This compression is seen in the upward escape of gas bubbles and streaks of fine ash from the compressed flow region. The lowermost, up to c. 0.03 m-thick (for the small ridge) and up to c. 0.2 m-thick (for the large ridge) region of converging and accelerating flow forms a distinct 1–1.2 m long jet-like structure ('J' in Fig. 6e-h). This 'jet' forms the base of the detaching flow behind the crest and is clearly visible in plots of the downstream (U) components of velocity and velocity magnitude (Figs. 6g-h).

Velocities in the diverging jet increase with obstacle size and reach values of up to 10 m s^{-1} in experiment L. In the detached flow above the jet, local flow velocities are up to 16 m s^{-1}. The presence of the visibly denser and fast-moving jet-like structure appears to shield the turbulent wake from particles sedimenting into it from the detached flow. The jet and detached flow in these experiments, however, does not entrain enough air to become buoyant (Andrews and Manga, 2012). Instead, over time the jet both diffuses downstream and alternately collapses (Fig. 6a-d), leading to the formation of finger-like instabilities protruding vertically downwards into the wake. During the times when the jet diffuses and collapses, ash-rich material sediments into the wake. The formation and collapse of the jet occurs episodically. In experiment S, we counted three jets, which are associated with velocities of up to c. 5 m s^{-1}. In experiment M, there are five phases of jet formation and collapse with maximum jet velocities of up to c. 8 m s^{-1}. For experiment L we counted only two prolonged jet phases with the largest velocities of c. 10 m s^{-1}. At least for the large obstacle, these velocity values are significantly higher than velocity maxima in the incoming flow and are distinctive features of the local compressible dynamics of the flow.

3.2.3. Phase 3

During approximately the second half of the passage of the gravity current body, the depth-integrated density markedly increases to values up to c. 20 kg m^{-3} (Fig. 2a and 3a). On the stoss side, the underflow reaches its maximum thickness, and, from c. 3 s, rapidly deposits a thick wedge of sediment (Fig. 7a and e). The continuing convergence and

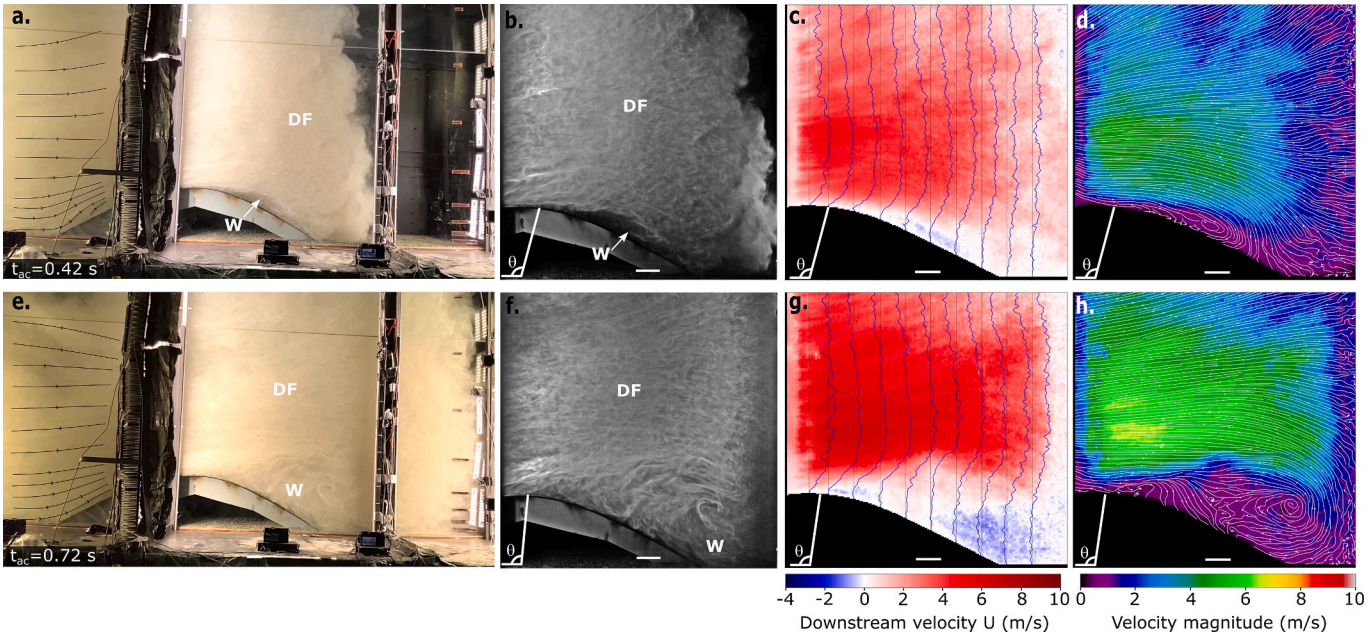

Fig. 5. Flow structure and velocity fields during passage of the density current head region (Phase 1) across the ridge for experiment M at two different times after flow front arrival at the crest t_{ac}. (a, e) Overview of the flow across the obstacle with flow streamlines drawn on the stoss side. 'W' marks turbulent wake and 'DF' the detached flow. White tick marks on the window frame are separated by 0.1 m. (b, f) Close-up view of the flow downstream from the crest recorded with a high-speed camera. The detachment point and angle are also shown. (c, g) Contour plots of the downstream velocity component U with vertical velocity profiles at intervals of 0.1 m. Note the occurrence of upstream and downstream rotating spot vortices during formation of the turbulent wake (c), which grow and migrate downstream through the wake (g). (d, h) Contour plots of velocity magnitude with streamlines overlaid on the image. Note the divergence of streamlines in the detached flow. The horizontal white bar at the bottom of columns two to four represent 0.1 m.

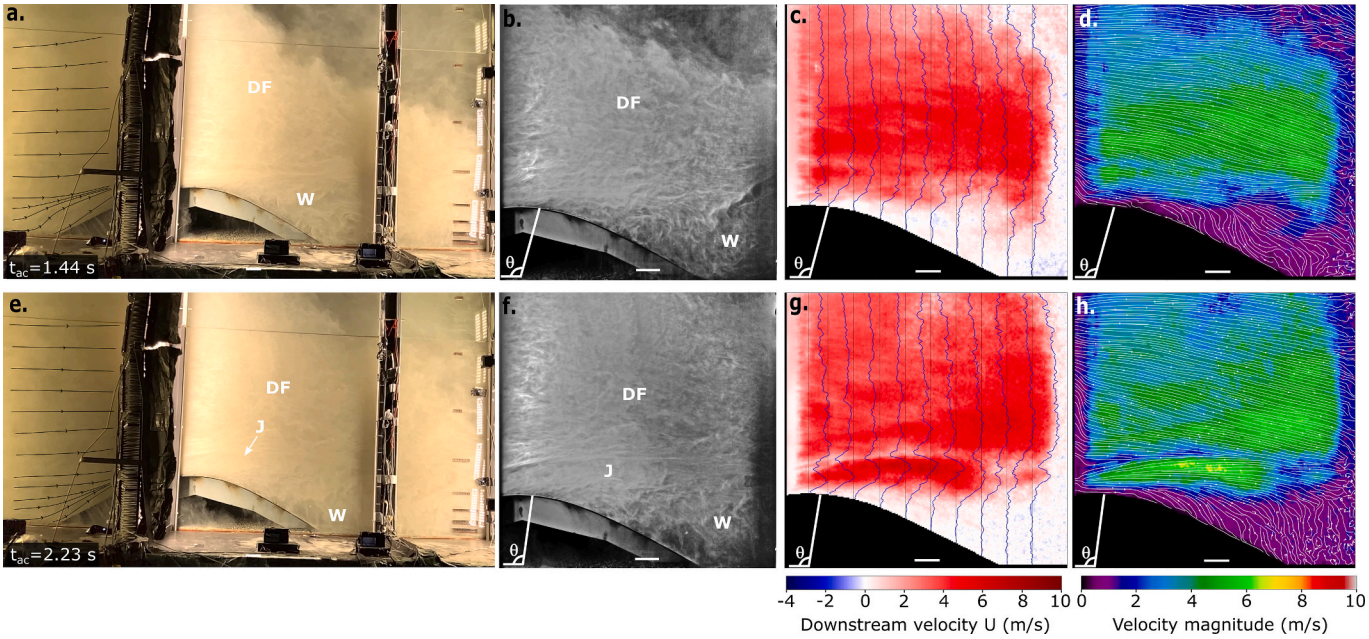

Fig. 6. Flow structure and velocity fields during passage of the proximal body region (Phase 2) across the ridge for experiment M at two different times after flow front arrival at the crest t_{ac}. The figure composition and velocity parameters are the same as in Fig. 5. 'J' marks the jet-like structures that repeatedly form and collapses as increasingly more concentrated flow arrives and interacts with the ridge, 'W' marks turbulent wake and 'DF' the detached flow. (a-d) Flow structure and velocity fields during a time when the jet has collapsed. Velocities inside the wake are low (10^{-2} to 10^{-1} m.s^{-1}) with variably upstream and downstream rotating, decimetric vortices. Velocities inside the detached flow are markedly higher (10^{0} m.s^{-1}) than inside the wake. Velocity maxima occur at a height of c. 0.3 m from the base of the detached flow. (e-h) Flow structure and velocity fields during a time of jet occurrence. At the base of the stoss side (e), flow streamlines steepen and strongly converge. The jet-like structure forms the basal and fastest region of the detached flow. Its upper and lower boundaries are sharp and characterised by strong shear gradients into the detached flow above and into the wake below.

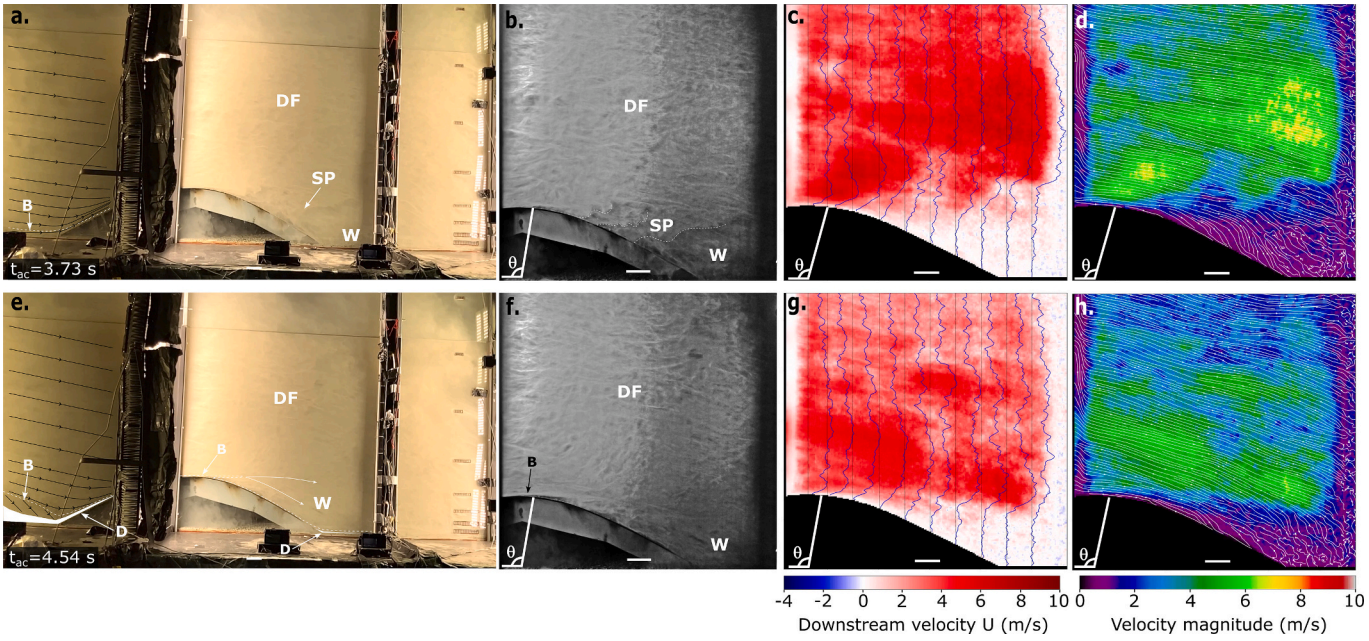

Fig. 7. Flow structure and velocity fields during passage of the distal body region (Phase 3) across the ridge for experiment M at two different times after flow front arrival at the crest t_{ac}. The figure composition and velocity parameters are the same as in Fig. 5. The dashed white line marks the upper boundary of the bedload region (B). Deposit (D) is highlighted in white. 'W' marks turbulent wake and 'DF' the detached flow. (a & e) On the stoss side, and with the arrival of increasingly more concentrated flow, the thickness of the bedload region increases and transitions into a coherent dense underflow causing rapid deposition. (b & f) At the base of the increasingly more concentrated detached flow finger-like instabilities develop and cause increased sedimentation into the wake as sedimentation pulses (SP). At times, the bedload reaches the crest of the hill and is re-suspended both into the wake and into the detached flow. (c, d, g, h) As the detached flow pushes onto the wake, the wake area begins to decrease.

acceleration of the flow advects dense flow material (including coarse, small- to medium lapilli-sized particles) from the lower wall region of the current into upper flow regions. Behind the crest, this loading of the detached flow with (coarse and heavy) particles bends the detached flow downwards (Fig. 7c, d, g, h). During this time, rolling and saltating particles as well as thin granular avalanches start migrating as a poorly-defined bedload over the crest and down the lee slope (Fig. 7f), while sedimentation pulses inside the wake become stronger (Fig. 7b). This coincides with a strong increase of the detachment angle up to 140° (Fig. 9b) and a decrease of the re-attachment distance (Fig. 9c), and thus a decrease of the cross-sectional area of the turbulent wake (Fig. 9d). Unlike in Phase 2, jet-like structures do not form in Phase 3. Instead, the strong disruptions of the vertical density and velocity structure are associated with enhanced sedimentation of particles into the increasingly hotter and denser turbulent wake (see also Supplementary Material 3).

3.2.4. Phase 4

From c. 5–6 s after flow arrival, the measured velocity and density of the incoming flow start to decrease, marking the passage of the gravity current tail region. The burial of the stoss side slope continues from the previous phase and decreases its effective slope as well as the effective obstacle height (Fig. 8a and e). As a consequence of the thick deposits, the wall region of the impinging density current ceases to converge and accelerate along the increasingly flatter stoss side of the obstacle. At the same time, while the downslope component of the velocity fields decreases, the vertical velocity component becomes more dominant. Together with the continuing sedimentation of particles from the upper flow into the turbulent wake, this leads to a distinct rotation of the velocity streamlines in the incoming and detached flow, from a previously slope-parallel direction (that is c. 6° from the horizontal) to angles similar to the lee slope of the obstacle (Fig. 8 a and e). This rotation of the flow field increases the angle of attack of the incoming flow onto the hill, increases the detachment angle as well as decreases the re-attachment distance and cross-sectional area of the turbulent wake (Fig. 8a-d). From c. 5.5–6 s, flow detachment ceases completely and the re-attached gravity current directly moves down the lee slope (Fig. 8e-h).

3.3. Geometric characteristics of the turbulent wake behind the obstacle

Fig. 9 characterises the temporal evolution of the turbulent wake that forms in all three experiments behind the hill crests. Time-series of the detachment angle θ, the re-attachment distance D_R and the cross-sectional area A_W of the wake are displayed (Fig. 9a). As expected for highly unsteady, high Reynolds number gravity currents, θ, D_R and A_W show strong turbulent fluctuations too (Fig. 9b-d). Despite these fluctuations, there are characteristic patterns of the temporal variations of these three geometric parameters in the four subsequent but highly transient flow phases.

The passage of the dilute PDC heads in Phase 1 are characterised by initial strong increases in θ, D_R and A_W associated with the frontal and central head regions, and their subsequent decreases during passage of the rear of the head and frontal body regions (Fig. 9b-d).

At slightly increasing flow density during Phase 2, θ, D_R and A_W alternatingly increase and decrease (Fig. 9b-d). These alternations correlate to the formation and collapse of the high-velocity jet-like structures at the base of the detached flow. For experiment M, with a crest height similar to the height of the velocity maximum of the incoming flow, the smallest detachment angles were observed.

With the arrival of a dense underflow before the obstacles during Phase 3, the detachment angles increase again, but also show fluctuations particularly for experiment L (Fig. 9b). This is associated with the largest upward spreading of the detached flow. The re-attachment distance and consequently the wake area, however, remain relatively constant or decrease (Fig. 9c-d).

The strong rotation of the flow field in the detached flow behind the crest during Phase 4 (Fig. 8), and passage of the significantly more dilute PDC tail region, are associated with strong increases of θ, which reach its maximum values (Fig. 9b). This is associated with the increase of the angle of attack of the PDC immediately above the hilltop and above the lee slope. The angle of the 'late' detachment leads to lower re-

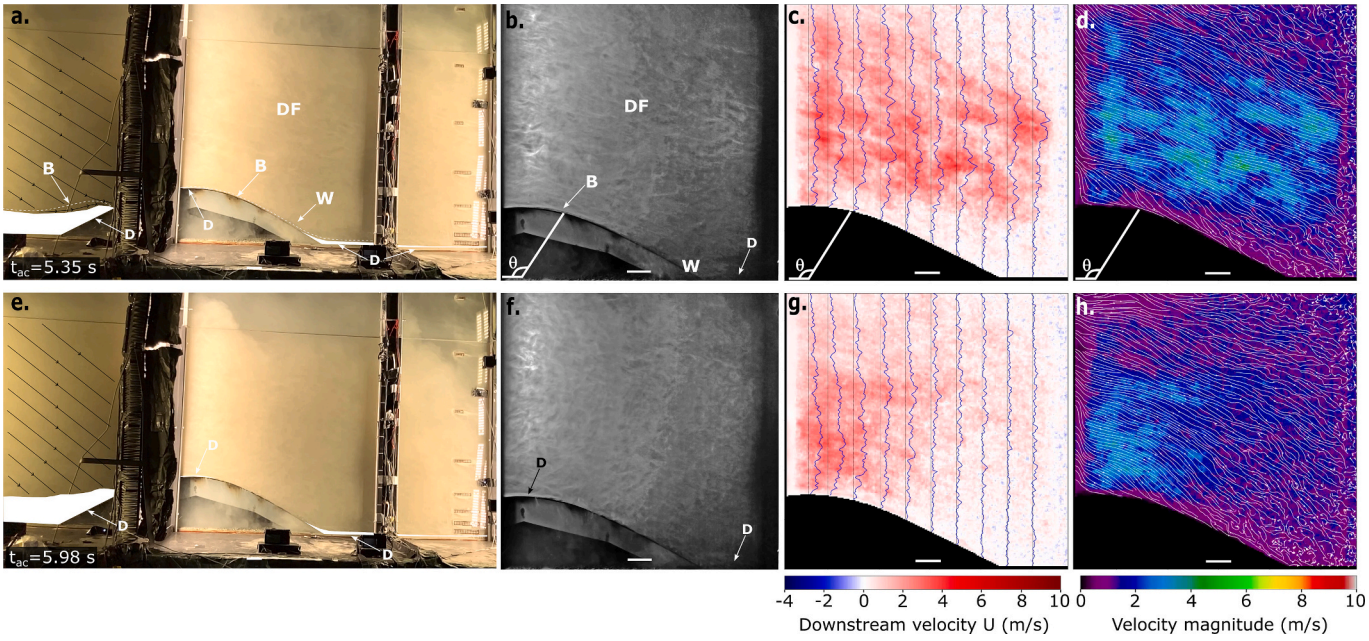

Fig. 8. Flow structure and velocity fields during passage of the tail region (Phase 4) across the ridge for experiment M at two different times after flow front arrival at the crest t_{ac}. The figure composition and velocity parameters are the same as in Fig. 5. (a-d) As flow velocity decreases and orthogonal velocity components become more dominant, flow streamlines rotate and become increasingly more parallel to the lee side slope. The detachment angle strongly increases, and the wake is about to disappear. 'B' highlights the bedload, 'D' corresponds to the deposits, 'W' marks turbulent wake and 'DF' the detached flow. (e-h) The flow has almost entirely passed. Flow detachment ceases and the flow fully adheres and moves down the lee slope.

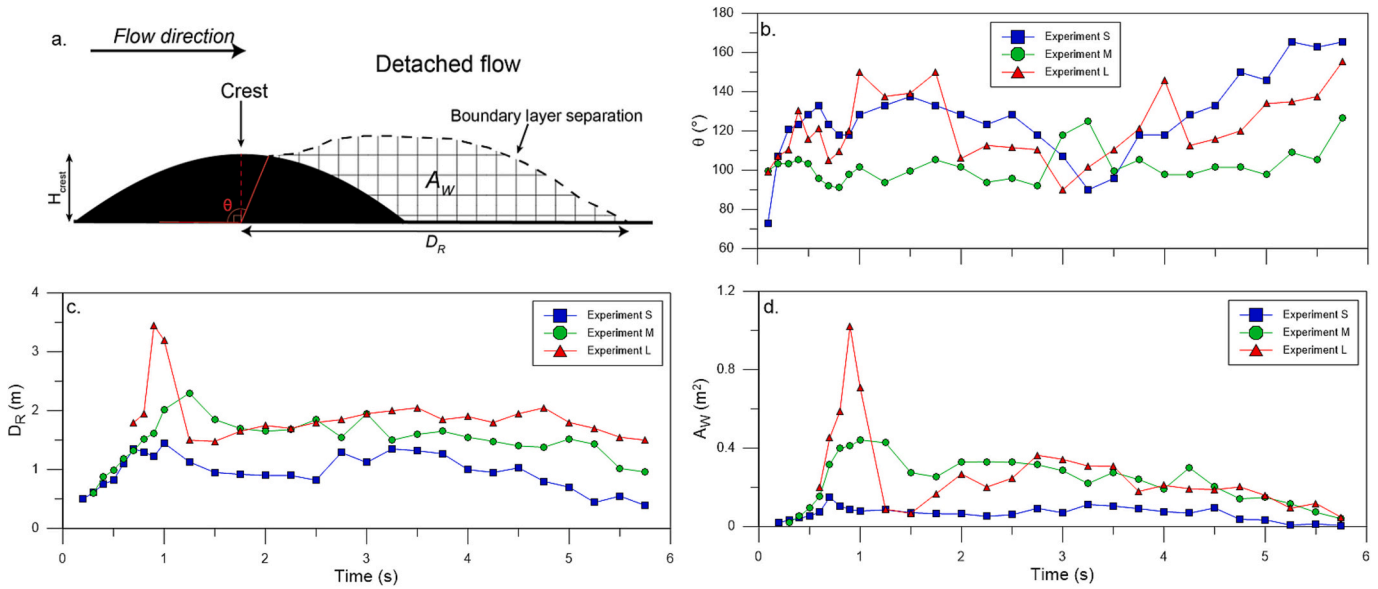

Fig. 9. (a) Sketch defining the re-attachment distance D_R, detachment angle θ and wake area A_W. (b-d) Time-varying detachment angle, re-attachment distances and wake area for each experiment. Note the strong decrease in the re-attachment distance and wake area after approximately 5 s of propagation as the detachment angle strongly increases.

attachment distances in the wake area during Phase 4 (Fig. 9c-d).

3.4. Spatiotemporal deposition and deposit characteristics

The sedimentary characteristics of the deposits of the three experimental PDCs were studied in relation to the spatiotemporally variable flow structure using high-speed videos, measurements of timeseries of local deposition rates, and sedimentological description of the time-resolved sampling and grain-size analysis of deposits. To describe the spatiotemporal deposition processes and to relate these to the spatiotemporally variable characteristics of the deposits across the obstacles, these observations and measurements are reported across a set of three figures (Figs. 10–12).

Fig. 10 presents the deposit thickness and structure across the obstacles. Examples of the main contrasting conditions of near-bed particle-gas transport and deposition that occur during flow passage across the obstacles are illustrated in Fig. 11. Fig. 12 shows a schematic of the different deposition environments across the obstacle, as well as timeseries of the deposition rate at different locations.

Overall, the experimental deposits are characterised by an asymmetry relative to the obstacles (Fig. 10a) with >0.1 m- and up to 0.23 m-thick deposits before the obstacle, which strongly thin to c. 20–80 mm thicknesses along the stoss side. This contrasts with *c.* 3–8 mm thick deposits above the crest and in the region of detached flow downstream of the crest. At the downstream end of the wake, where intermittent and finally complete flow re-attachment occurs, deposits thicken again to *c.* 10–18 mm. Despite the same experimental starting conditions, the thickness variations upstream of the obstacle and onto the stoss side differ between the three experiments (Fig. 10a). While, in experiment S, the deposit generally thins towards the obstacle, in experiments M and L, deposit thicknesses are more uniform or even slightly thicker towards the obstacle. This is related to our experimental design, and due to the smaller distance between the impact zone and the stoss side of the obstacle with increasing obstacle size. This design condition results in the stranding of frontal lobes of the dense underflow before the obstacle in experiment S, and increasingly stronger interaction and partial encroaching onto the stoss slope of the underflow in experiment M and even more so in experiment L. Despite these design-related differences between the three experiments, the general deposit architecture and the general parental flow and deposition conditions are similar in each of the three studied situations, as described in the following sections.

3.4.1. Spatiotemporal deposition before the crest

During passage of the PDC head (Phase 1), strong basal shear leads to intermittent, minor, deposition and erosion events associated with tractional bedload transport at the flow base by rolling and saltation. This results in generally no net deposition until the obstacle (Fig. 10b). Only in experiment L, millimetric, laminated ash layers onlap onto the lower stoss side of the obstacle.

During passage of the frontal body region (Phase 2), characterised by increasing density stratification and (depth-averaged) flow density, the thickness of the bedload layer increases to *c.* 1–3 cm (Fig. 2a). This is associated with more vigorous particle rolling and the formation of intermittent dense granular avalanching, a bedload process referred to as 'granular sand waves' in Brosch and Lube (2020). The granular avalanches grow in thickness and duration over time, emplace *c.* 1–3 cm thick, massive beds before the obstacle (Figs. 10b and 11a) and grade into laminated ashes on the stoss slope at characteristically uniform deposition rates of *c.* 1–2 mm s^{-1} (Fig. 12b stoss side).

During Phase 3, with formation and subsequent arrival of the dense underflow (Fig. 2a), intermittent (centimetre-long) granular avalanching transitions into a coherent, highly mobile, dense, granular-fluid underflow. For most of its motion towards the obstacle, the underflow obeys strong basal slip at the lower flow boundary. At *c.* 3 s after flow arrival, as frictional stresses start to dominate over hydrostatic stresses (c.f. Lube et al., 2019), basal slip vanishes and deposition occurs at the base of the underflow (Fig. 11a, right column, '①') at high rates of up to 180 mm s^{-1} (Fig. 12b profile 1). Against the obstacle, this emplaces successive and partially overlapping lobes of the underflow. The resulting deposits are *c.* 3–15 cm-thick and massive, with upstream-correlatable bedforms of very fine ash to medium lapilli (Fig. 11a, left column, '①'). This polymodal and very poorly sorted *pumice breccia* (Fig. 11a, middle column, '①') lacks strong vertical grading, and is a clast-supported facies. These local facies variations are characterised by a coarse-tail grainsize grading of pumice lapilli. High-speed videos of the emplacement of the pumice breccia show that the pumice breccia facies records the consecutive emplacement of underflow pulses with coarse-grained fronts and tops and more ash-rich interiors that result from size segregation of pumice lapilli relative to the ash-rich matrix (c.f., Lube et al., 2007).

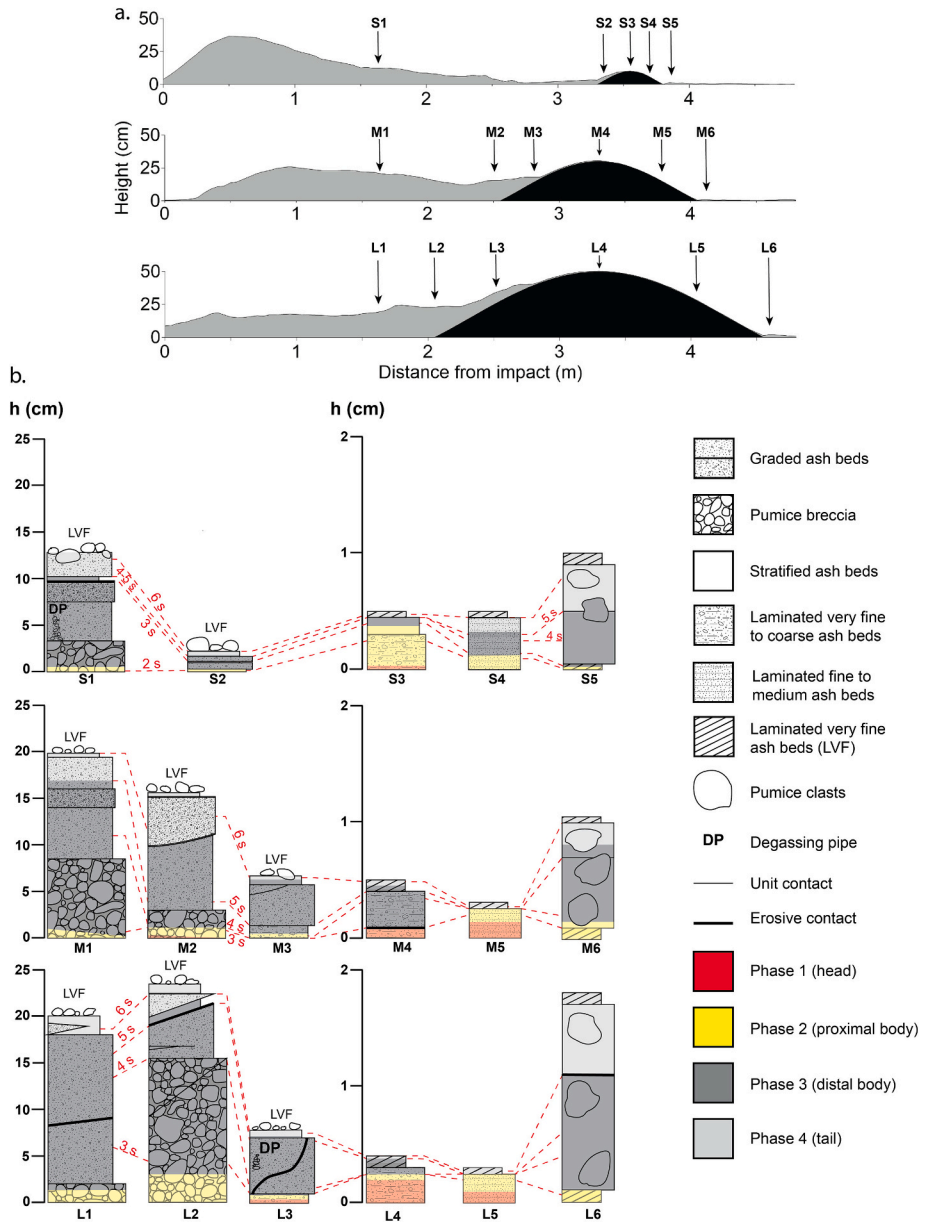

Fig. 10. Measurements of the variation in total deposit thicknesses and structure across the obstacles. (a) Deposit thickness against distance for the first 4.8 m of the channel for experiments S, M and L. The labelled arrows indicate the positions of vertical deposit profiles shown in (b). They show the positions of closely examined, slope-perpendicular deposit profiles that are located before the obstacle and on the stoss slope of the obstacles (locations labelled S1–S2, M1–M3 and L1–L3 for experiments S, M and L, respectively), above the crest (locations S3, M4 and L4), on the lee slope below the turbulent wake (locations S4, M5 and L5), and at a location at the downstream end of the turbulent wake where intermittent re-attachment occurs (c.f., section 3.1; locations S5, M6 and L6). (b) Vertical deposit profiles for the three experiments located between Profile 1 and the end of the obstacle. Different deposit facies are colour-coded with respect to the parental flow regions that are associated with their emplacement. The red dashed lines mark isochrones of deposition as time after flow front arrival. (For interpretation of the references to colour in this figure legend, the reader is referred to the web version of this article.)

The massive breccias are conformably overlain by three to four, several centimetres-thick, massive to vaguely stratified and normally graded beds of very fine ash to fine lapilli (Fig. 11a, left column, '②'). These very poorly sorted *graded ash beds* contain lower amounts of coarse pumice lapilli than the underlying pumice breccia bedforms (Fig. 11a, middle column, '②'). Successive beds become increasingly finer-grained and contain progressively fewer high-density lithic particles. At their tops, each of these bedforms conformably grade into millimetric, laminated very fine to fine ash (labelled 'A' in Fig. 11a left '②'). Each of these bedforms is emplaced by several centimetres-thick pulses of dense, fluidized ash-rich, granular-fluid underflow (Fig. 11a, right column, '②') and at sedimentation rates of *c.* 50 mm s^{-1} (Fig. 12b, Profile 1).

The passage of the end of the PDC body and tail regions are associated with initially high, but continuously decreasing (depth-averaged and basal) flow velocities and densities (Figs. 2 and 3), and decreasing ranges and mean particle sizes of transported solids (not shown). This coincides with the vanishing of the coherent dense underflow and transitioning (back) into bedload transport of alternating highly fluidal granular avalanching and tractional bedload with particle rolling. These alternating bedload processes emplace several centimetres-thick, highly stratified and partially cross-bedded, and vaguely normally graded *stratified ash beds* of very fine-ash to coarse ash (Fig. 11a, left column, between '②' and '③'). The boundary between graded ash bed and

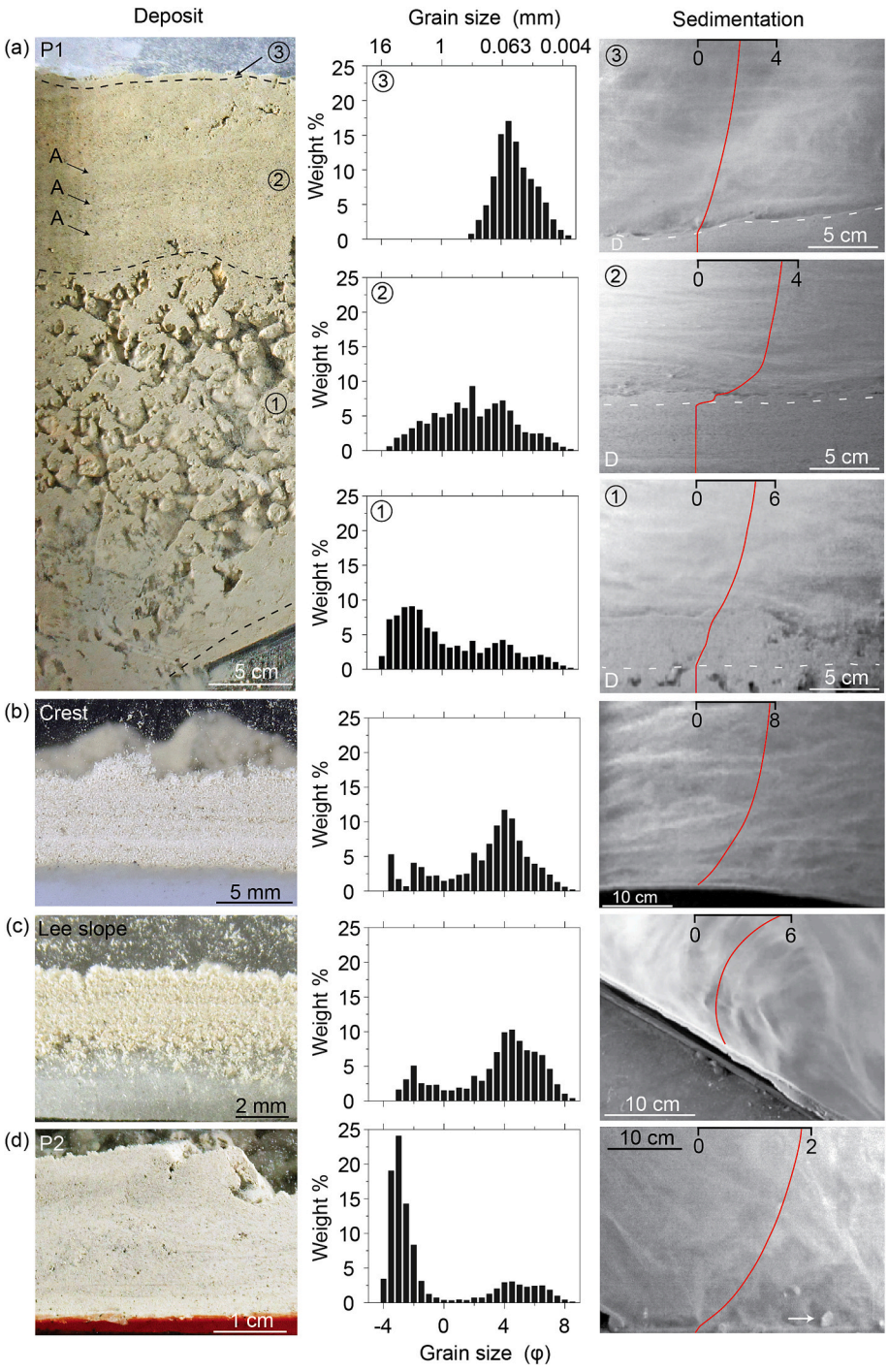

Fig. 11. Main contrasting conditions of near-bed particle-gas transport and deposition in front of the obstacle (a), above the ridge crest (b), along the lee slope (c) and downstream of the obstacle (d). The left column shows close-up photographs of the deposits in these four locations. In (a) black dashed lines highlight bed boundaries between poorly sorted pumice breccia (denoted '1'), graded ash-beds (denoted '2') separated by fine ash layers (denoted 'A') and laminated very fine ash facies (denoted '3'). The middle column shows grain-size distributions of the deposit facies shown on the left in histogram form. The right column depicts images from high-speed video recording during the time of deposition of the deposit facies shown on the left. The lower flow boundaries, separating the flow and deposit (denoted 'D') are highlighted by white dashed lines. Slightly time-averaged, slope-perpendicular velocity profiles determined by particle image velocimetry are shown as red curves. A description of near-bed particle-gas transport and deposition mechanisms is given in the main text. (For interpretation of the references to colour in this figure legend, the reader is referred to the web version of this article.)

stratified ash bed lithofacies is sharp and partially erosive (Fig. 10b), and, in the vicinity of the obstacles' stoss side, is sub-parallel to the stoss slope. Boundaries between individual bedforms of the stratified ash bed lithofacies are similarly inclined, and are associated with progressive back-stepping deposition with an upstream migrating deposition front (Supplementary Material 3). Slope-perpendicular deposition rates of these antidune-like bedforms of the stratified ash bed lithofacies ranges between *c.* 20–80 mm s^{-1} and decrease with time (Fig. 12b, Profile 1).

Waning flow in the PDC tail region (Phase 4) is associated with tractional bedload transport and rolling of pumice lapilli at the base of the wall region's boundary layer (Fig. 11a, right column, '③') at declining flow velocities and densities (Figs. 2 and 3). This emplaces

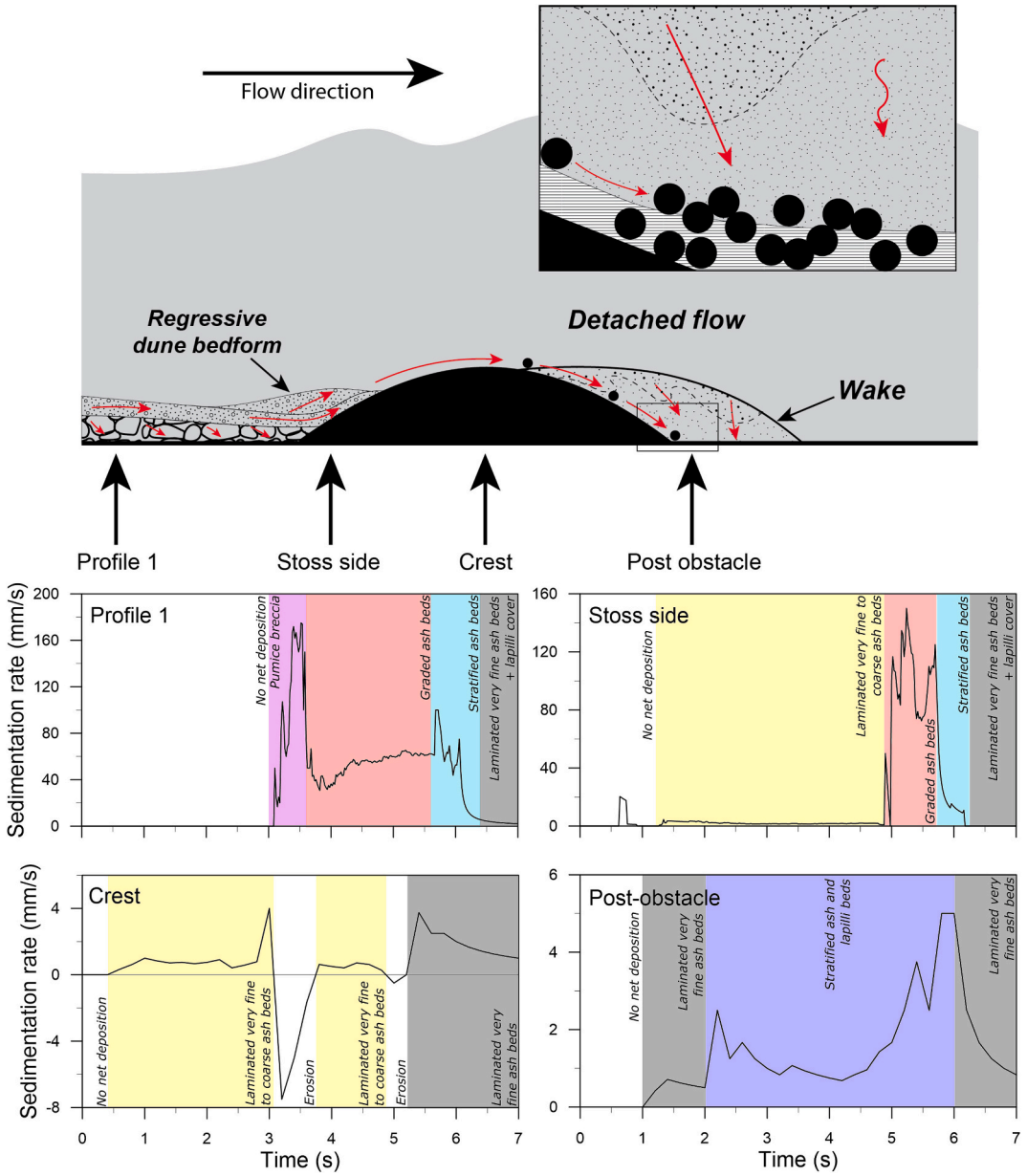

Fig. 12. Sedimentation across obstacles. (a) Schematic figure showing the sedimentation environments across the obstacle. The red arrows indicate sedimentation transport direction. On the stoss side, the underflow is blocked and regressive dune bedforms are built. Upon crossing the hill, the sedimentation processes inside the wake are represented in the inset, showing non-detaching bedload flowing down the lee slope and getting stranded, fast particle settling from finger-like instabilities and slower tractional sedimentation from the peripheries of shear-induced eddies. The profiles shown in (b) are indicated. (b) Time-series of deposition rate for four locations across the obstacle for Experiment M. The rates vary by several orders of magnitude between locations. Colors code the different sediment facies deposited. (For interpretation of the references to colour in this figure legend, the reader is referred to the web version of this article.)

sub-millimetric, very fine ash-dominated (Fig. 11a, middle column, '③'), unimodal and well-sorted laminated ash beds. These contain and are covered by abundant, stranded rolling pumice lapilli (Fig. 11a, left column, '③'). The *laminated very fine ash beds* conformably overly and mantle the stratified ash bed lithofacies. They are associated with significantly lower deposition rates than any of the earlier emplaced bedforms, of *c.* 1 mm s^{-1} (Fig. 12b profile 1 and stoss side) The laminated very fine ash beds are the only bedforms that produce a continuous deposit across the obstacles (Fig. 10b), and across the entire PDC runout.

3.4.2. *Spatiotemporal deposition above the crest*

Above the crest, the experimental PDCs emplace a *c.* 3–5 mm thick sequence of thinly *laminated very fine- to coarse-ash* (Fig. 10b and Fig. 11b, left column). The bulk-sampled sequence is a polymodal, very poorly sorted lithofacies (Fig. 11b, middle column). It is composed of up to seven, laterally non-continuous, millimetric to sub-millimetric, and internally normally graded lamina. Overall, there is a continuous vertically upwards fining from one lamina to another.

The depositional environment consists of a fully attached, turbulent boundary layer flow (Fig. 11b, right column). Strongly time-varying fluctuations in flow velocity and density in the basal flow coincide with strong variations in the thickness of the bedload region. Unlike upstream of the obstacle and on the lower stoss slope, the experimental PDCs has already started to deposit during passage of the PDC head (Phase 1). Once a bedload starts to develop, during passage of the rear of the head region, and throughout the passage of the frontal body (Phase 2), deposition occurs through a combination of tractional and rolling

bedload transport, at an approximately constant deposition rate of *c.* 1 mm s^{-1} (Fig. 12b, crest).

Passage of the increasingly denser middle to distal body regions of the PDCs (Phase 3) leads to a sudden quadrupling of deposition rate, which is immediately followed by a *c.* 1-s-long erosive event (Fig. 12b crest, *c.* 3–4 s). This leads to erosion of the previously emplaced ash laminae except for remnants that remain intact inside the interstices of the glued-on surface roughness. The erosion event(s) coincides with the high-velocity and high-density flow during formation and passage over the crest of the jet-like structures (c.f., section 3.2.2). At the end of Phase 3 (Fig. 12b crest, *c.* 4–5 s), deposition starts again at very low rates of *c.* 0.5 mm s^{-1} through a combination of tractional bedload transport and rolling of coarse ash to small lapilli-sized particles. Following a brief, second erosion event (Fig. 12b crest, *c.* 5 s), and during passage of the PDC tail region (Phase 4), the deposition rate suddenly increases to *c.* 4 mm s^{-1} before exponentially declining during waning flow conditions.

3.4.3. Spatiotemporal deposition below the detached flow

The deposits downstream from the crest capture sediment transport and deposition inside the turbulent wake beneath the detached flow (along the lee slope of the obstacle), and at the downstream periphery of the turbulent wake (mostly behind the obstacle) where flows intermittently and later fully reattach (c.f., sections 3.2 and 3.3).

Along the lee slope, the deposits are *c.* 3 mm-thick (Experiment S) to c. 5 mm-thick (Experiment L), consisting of very thinly laminated, fine- to medium ash (Figs. 10b and 11c, left column). The individual, sub-millimetre-thick lamina are discontinuous and characterised by erosive boundaries between laminae. These bulk-sampled, *laminated fine- to medium-ash* have strongly bimodal and very poorly sorted grain-size distributions (Fig. 11c middle). In comparison to the laminated very fine- to coarse ash deposits above the crest, the bimodality in lee slope deposits is more pronounced (*c.f.*, Figs. 11b-c middle column). Time-averaged deposition rates along the lee slope are the lowest anywhere across the obstacle and are well below 1 mm s^{-1}. With increasing obstacle height, the time-averaged deposition rate increases systematically from *c.* 0.3 mm.s^{-1} (Experiment S), to *c.* 0.5 mm.s^{-1} (Experiment M) to *c.* 0.7 mm.s^{-1} (Experiment L).

Immediately *downstream of the obstacle*, the millimetres-thick, very thinly laminated fine- to medium-ash lee slope deposits transition into *c.* 1 cm-thick (Experiment S) to *c.* 2 cm-thick (Experiment L) thickly laminated *stratified ash and lapilli beds* (Fig. 10b and 11d, left column). The bulk-sampled deposits are characterised by a pronounced bimodality with a dominant coarse-tail mode at *c.* 8 mm (3 Φ) and a more uniform fine-tail mode around *c.* 50 μm (Fig. 11d, middle column). In comparison to crest and lee slope deposits, the stratified ash and lapilli beds contain larger proportions of coarse ash to medium lapilli and lower amounts of finer-grained ash fractions. Deposition commences during Phase 2, when the frontal body region passes in the detached flow above the wake, at initially low rates of less than 1 mm s^{-1} (Fig. 12b, post-obstacle). During Phase 3, and in particular when intermittent flow re-attachment occurs *c.* 4.7 s after flow arrival, the deposition rate increases strongly to *c.* 5 mm s^{-1}, before exponentially declining again during Phase 4 of the waning flow (Fig. 12b).

Despite the seemingly simple bedform characteristics of the deposits emplaced below the detached flow, deposition involves three different, and in part simultaneously occurring, mechanisms.

First, while flow detachment occurs downstream of the crest, particles transported as bedload do not detach and instead continue rolling down the lee slope (Fig. 12a). These dominantly coarse ash- and lapilli-sized particles deposit along the lee slope and in the zone immediately after the obstacle. Over time, this emplaces a several centimetres-thick and stratified scree-like deposit. This local deposit facies contains abundant lapilli clasts, forming the coarse mode in the middle column of Fig. 11d.

Second, the strongly vortical flow inside the wake (c.f., sections 3.2 and 3.3 and Figs. 5c and g) is characterised by variably upstream- and downstream rotating and migrating turbulent structures. This leads to variably, upstream- and downstream-directed tractional deposition from the peripheries of the turbulent structures (Fig. 11c, right column).

Third, during Phases 2 and 3, strong shear of the base of the detached flow with the turbulent wakes leads to fast settling through the wake of finger-like instabilities (Fig. 12a; section 3.2). These fingers have visibly higher particle concentrations than adjacent 'non-fingered' regions in the wake and sediment faster through the wake than turbulent background sedimentation inside the coherent turbulent structures. These second and third mechanisms emplace the laminated, fines-rich stratified layers in the wedge where lapilli are stranded, forming the fine mode in Fig. 11d.

The relative contributions of these three distinct deposition mechanisms (i.e., bedload migration into the wake; turbulent, tractional deposition; and fast settling from instabilities) varies in both space and time across the wake but cannot be quantified accurately with our images and sampling of deposits.

4. Discussion

The experimental analogues provide guidance for understanding transport and sedimentation processes in natural PDCs over obstacles. First, however, we consider two differences between natural and experimental currents. In terms of bulk flow characteristics, the experimental analogues scale well to natural PDCs (Table 1). However, experimental and natural flows differ in the absolute values of their characteristic length- and time-scales, while using pyroclasts with a comparable or only slightly finer grained size range. Geometrically scaling the finest particle sizes in experiments would yield particles with diameters below 1 μm. This would result in cohesive effects that are not characteristic for natural PDCs. Such scaling imperfections may lead to scaling differences on small scales and in the relative duration (and effectiveness) of individual multiphase transport, particle settling and deposition processes. The effects of scaling imperfections across all scales are not well understood, but we suspect that they can result in differences in textural deposit characteristics and aspect ratios of bedforms.

A second difference concerns the variable mobility of concentrated, granular-fluid transport regimes that form at the base of PDCs (Breard et al., 2018). In our experiments, with moderate hopper mass discharge rates, dense underflows remain relatively immobile, and they become fully blocked by obstacles of all tested sizes. In experiments without obstacles and similar discharge rates, the frontal lobes of these underflows would terminate at c. 6–7 m, that is c. 2–3.5 m downstream of the obstacle. This, however, does not imply that dense flow regions in experimental and natural PDCs would inevitably become fully blocked by obstacles under similar ratios of flow depth to obstacle height. For instance, at the conditions of high hopper mass discharge, resulting very mobile underflows propagate up to 26.5 m (Lube et al., 2019) and can also move upslope on inclines to heights above the channel base that are comparable to the height of at least the smallest tested obstacle. To address this point, future physical or numerical experiments should explore the topography interaction of PDCs with underflows of variable thickness, velocity and gas pore-pressure. Furthermore, in this study, the Froude number of the ash-cloud surge region of the experimental PDCs was characterised by a balance of inertial and gravitational forces. Systematic experiments with flows over variably inclined substrates, and with obstacles placed into different runout reaches (e.g., where buoyancy forces and/or air-drag become significant (Brosch et al., 2022) would be worthwhile to investigate the control of the Froude number on PDC-obstacle interaction.

4.1. Flow perturbation by PDC transport across ridges

Our experiments show that the interaction of PDCs with ridges generates a strong local perturbation of the internal flow structure. To a

first order, this is due to the occurrence of three successive processes: the blocking of the lower, concentrated flow region in front of the obstacle; the compression and acceleration of the intermediate and upper flow regions on the stoss side; and the flow detachment behind the crest and formation of a turbulent wake.

The most pronounced flow change is the reduction in mass flux due to the blocking of the underflow. The deposition before the crest associated with the underflow blocking is similar for all obstacle sizes and accounts to up to 90 % of the initial mass. The time- and depth-averaged velocity $\overline{U}$ of the non-blocked flow regions also decreases. The loss in velocity between profiles 1 and 2, $\Delta\overline{U} = (\overline{U_1} - \overline{U_2})/\ \overline{U_1}$ is c. 31 % for experiment S, c. 23 % for experiment M and c. 12 % for experiment L and is thus inversely related to the crest height of the ridges. This inverse relationship is qualitatively explained by the acceleration of the flow during compression along the stoss slope. The rate of acceleration increases with increasing ridge height as the projected area of the obstacle, i.e., the product of crest height and flow width, increases. In experiment L, velocities in the compressed and accelerated flow are at least 2–3 times larger than local velocity maxima in the flow before the obstacle. This observation implies local increases in dynamic pressure on ridge stoss slopes by a factor of c. 4–9. It also highlights the importance of using highly-resolved compressible multiphase flow models to accurately predict local variation in PDC hazard intensities.

Flow detachment behind the crest generates another main perturbation to the vertical flow structure. The formation of a turbulent wake of an initial volume of ambient air underneath the detached flow results in an unstable vertical density stratification. After flow re-attachment downstream, the vertical density stratification needs to redevelop. This takes longer for larger obstacles because the disturbances to the flow are greater.

The variability in velocity and density across the PDC head, body and tail flow regions has a second order control on the flow perturbation. The effects of this variability include variations in the deposition rate (see further discussion below); the occurrence of repeated events of acceleration and formation of jets along the stoss side and over the crest due to velocity and particle concentration changes during passage of the largest coherent turbulence structures; and the time-varying changes of the detachment angle, the geometry of the turbulent wake, and the location of flow re-attachment behind the crest.

Guinn et al. (2022) envisaged different detachment behaviours for the head and body regions of the Mount *St*. Helens blast to explain different degrees of tree damage on the lee side of ridges. There, the authors suggested that in medial to distal runout reaches, while the head was jumping over the hills, the body was more ground-hugging, destroying partly or totally the trees on the lee side of the hills. Under the conditions tested in our experiments, this would be comparable to our Phase 3, though a complete vanishing of flow detachment and an adhering of the PDC onto the lee slope only occurs during passage of the PDC tail region. The main controlling flow parameter appears to be the angle of attack of the PDC onto the ridge, which strongly steepens and approaches the inclination of the lee slope during the waning flow.

4.2. Deposit asymmetry across ridges

The experimental deposits emplaced across wall-mounted and ridge-shaped obstacles are governed by orders of magnitude differences in thickness on the stoss-side (decimetric), crest (millimetric) and lee side of obstacles (millimetric) and immediately downstream of the obstacle (centimetric). Measurements of the local time-varying deposition rates across the obstacle (Fig. 12) show that these deposit thickness variations are associated with variations in deposition rate that span by (at least) three orders of magnitude (i.e., 10^{-4} to 10^{-1} m.s^{-1}). The general pattern of deposit asymmetry observed in experiments closely resembles those measured in detailed isopach maps or systematic streamwise transects of deposits of historic, small- to intermediate volume PDCs of Mount *St*. Helens 1980 (Bursik et al., 1998), Merapi 2010 (Cronin et al., 2013) and Te Maari 2012 (Breard et al., 2015). Bursik et al. (1998) and Breard et al. (2015) documented the local thickening of deposits at the foot of a ridge followed by a thinning towards ridge crests, a decrease in deposit thickness on the lee slope before re-thickened deposits at the downstream end of the ridge. Based on the experimental observations, this pattern can be interpretated as the deceleration and blocking of the basal concentrated flow region in-front of the obstacle. This is followed by strong acceleration of the non-blocked upper flow region along the stoss side and towards the crest leading to a decrease in deposition rate alternating with short-lived periods of erosion. The sudden decrease and minima in deposit thickness behind the ridge crest in natural deposits is explained by low deposition rates inside the turbulent wake, while the detached flow does not directly contribute to local deposition processes. The final re-thickening towards the base of the ridge could be explained by the flow re-attachment at the downstream end of the turbulent wake and re-establishment of a strong vertical density stratification and bedload region.

4.3. Comparison between experimental and natural PDCs deposits across ridges

The PDC deposits of the Te Maari 2012 eruption provide well-documented examples for the architecture of deposits across 8–40 m high, flow-perpendicular ridges that were emplaced by a short-lived, strongly vertically stratified and dilute PDC (Breard et al., 2015). PDC deposits comprise distinct vertical successions on the stoss sides, crests and lee sides of ridges that, as described below, resemble the sedimentary facies emplaced by the experimental PDCs.

On the foot of ridges, the c. 0.5–1 m-thick deposits were comprised of basal, poorly sorted and upwards fining breccia (unit A) that are overlain by finer-grained and stratified beds (unit B) and an upper laminated fine ash (Unit C) (c.f., Fig. 3b' and e in Breard et al. (2015)). The tripartite vertical structure could be correlated onto the stoss side, where unit A progressively thins upslope and unit B shows up- and downstream migrating, partially cross-bedded bedforms of thickly laminated to thinly bedded medium ash to coarse lapilli (Fig. 13a location A for Te Maari, and Fig. 11a left column in experiments).

On ridge crests, the 2–5 cm-thick deposits are composed of laterally discontinuous, laminated to thinly bedded medium ash to lapilli with abundant erosive unconformities between layers (Fig. 13a location B). These deposits strongly resemble the experimental ridge facies of laminated fine to coarse ash (Fig. 11b, left column). In analogy to the experimental observations, they can be explained by alternating erosion and tractional aggradation events during by-passing of the PDC whose lower, partially blocked flow region becomes compressed and accelerated as streamlines converge.

On the lee side, centimetric fine to coarse ash occur as laterally discontinuous laminated beds, with abundant lenses of fine to medium lapilli (Fig. 13a location C). Texturally these coincide with the laminated very fine to medium ash emplaced at the base of the turbulent wake in experiments (Fig. 11c, left column) and can be explained by the synchronous deposition by tractional aggradation from the peripheries of shear-induced eddies inside the wake (the ash laminae) and of bedload migrating over the ridge (the discontinuous lenses). Breard et al. (2015) reported the occurrence of millimetre-thick ash deposits on leaves, with comparably thinner deposits directly on the ground underneath. This is indicating strong sedimentation onto the leaves from above, in comparison to relatively weaker traction sedimentation on the ground. This observation could indicate that, as in experiments, a third process of sub-vertical sedimentation from finger-like instabilities may similarly occur in the turbulent wake of natural dilute PDCs.

At Te Maari, like the blast deposits of Mount *St* Helens (Bursik et al., 1998), a sudden re-thickening of deposits occurred on the lower leeside of ridges. These locations coincide closely with a sharp boundary between a lee side zone of vegetation with little to no damage to leaves and

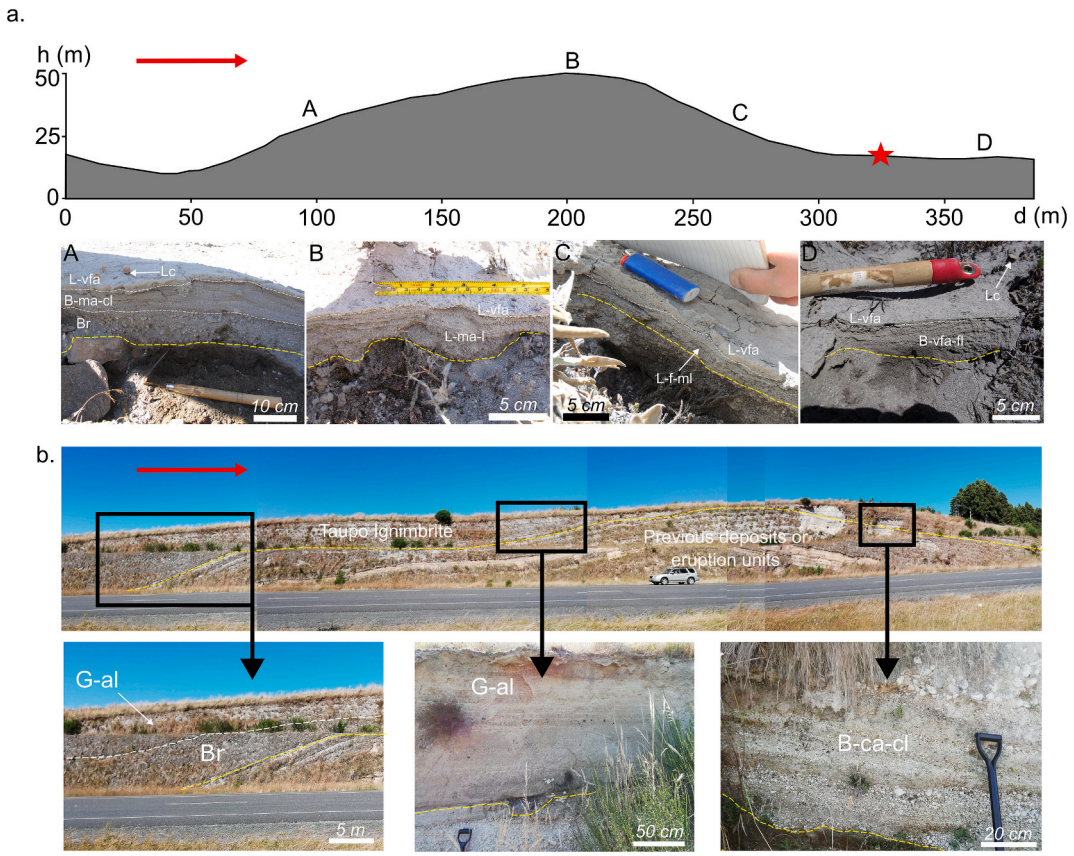

Fig. 13. PDC deposits across ridges at Te Maari and Taupo, New Zealand. Yellow dashed lines separate the eruptive unit from previous deposits, and white dashed lines separate deposition facies. Red arrows indicate flow direction. *Lc:* Lapilli cover; *L-vfa:* Laminated very fine ash beds; *B-ma-cl:* Bedded medium ash to coarse lapilli; *Br:* Pumice breccia; *L-ma-l:* Laminated medium ash to lapilli; *L-f-ml:* Laminated fine to medium lapilli; *B-vfa-fl:* Bedded very fine ash to fine lapilli; *G-al:* Graded ash and lapilli beds; *B-ca-cl:* Bedded coarse ash to coarse lapilli. (a) 2012 Te Maari hydrothermal blast-like PDC deposits (New Zealand). A topographic profile shows the first topographic obstacle encountered by the westerly directed PDCs at about 1000 m from the source. Letters indicate the location of the photos below. The red star shows the modelled re-attachment distance (Corna et al., 2025). The PDC deposits are approximately one order of magnitude coarser grained and thicker than in the experiments. Similarities between natural and experimental deposits are discussed in the main text. (b) 232 CE Taupo Ignimbrite (New Zealand). The composite photo shows an obstacle located 15 km from the inferred vent with continuous ignimbrite deposit across the obstacle. The zoomed-in photographs show bedforms that are one to two orders of magnitude thicker and coarser than the experiments. (For interpretation of the references to colour in this figure legend, the reader is referred to the web version of this article.)

twigs before a zone with stronger damage to vegetation, which was highly visible during field surveys and in satellite imagery. Corna et al. (2025) demonstrated that the lateral extent of the low-damage zone (red star in Fig. 13a), and thus the downstream lengths of the turbulent wake, can be predicted for natural and experimental PDCs through an empirical model linking the characteristic scales of the obstacle and the flow. The re-thickened Te Maari deposits emplaced in the zones of re-attached flow are 5–10 cm-thick sequences of lower massive beds and upper stratified beds of very fine ash to small lapilli (Fig. 13a location D). The textural and grain-size characteristics as well the strong re-thickening resemble the experimental deposits emplaced by the re-attached flow (Fig. 11d).

Fig. 13b shows exposures of the 232 CE Taupō Ignimbrite (New Zealand) emplaced across a c. 15 m-high ridge as an example of a significantly more sustained and longer lasting interaction of PDCs with a ridge than in the Te Maari and Mount St. Helens cases. This obstacle is located c. 15 km from the inferred vent in a northern direction and oriented approximately perpendicular to an inferred radial flow direction.

As the density current approaches the obstacle, the ignimbrite develops a tripartite structure with a decimetric basal groundlayer enriched in crystals and lithics, which is overlain by up to 8 m of massive pumice breccia of very fine ash to coarse lapilli, and an upper, up to 5 m sequence of massive, graded ash and lapilli beds that are separated by distinct centimetric layers of very fine ash (Fig. 13b). Similar to the experimental deposits, the pumice breccias terminate on the lower stoss side, while the massive ash beds progressively thin along the stoss side. From the crest onwards, deposits start showing stratification with coarse pumice lenses intercalated between finer-grained ash-rich layers (Fig. 13b). On the lee side, deposits are more strongly layered than on the crest. The pumice clasts in coarse pumice lenses are significantly more rounded than pumices in adjacent ash-rich layers.

Large ignimbrite deposits remain enigmatic with regards to hypothesized dominant particle-gas transport regimes of their parental PDCs as either a dense granular-fluid flow or a dilute turbulent suspension (e.g. Wilson, 1985; Dade and Huppert, 1996; Roche et al., 2016; Breard and Lube, 2017). Our experimental study does not attempt to provide an answer to this longstanding debate. However, the contrasting deposit facies across the obstacle shown in Fig. 13b are inconsistent with earlier interpretations of ground-hugging dense or dilute currents that adhere to a ridge-shaped topography (e.g. Druitt, 1998; Branney and Kokelaar, 2002). Instead, the similarities with the experimental deposits suggest that, at the base of the PDC, a region of dense fluidized granular current with a thickness of less than the height of the ridge occurred that became blocked by the ridge. Acceleration of the non-blocked upper and more dilute flow region would have led to flow detachment and formation of a turbulent wake behind the ridge crest. On the lee side, the strong rounding of pumice lapilli that occurs in coarse lenses is

consistent with bedload rolling and/or saltating over the ridge crest. Their alternation with stratified ash-rich beds suggests the occurrence of synchronous tractional deposition albeit at lower deposition rates akin to the tractional deposition from the peripheries of shear-induced eddies inside the turbulent wake in the experiments.

5. Summary and conclusion

The processes of transport and sedimentation of PDCs interacting with ridge-shaped obstacles were investigated in large-scale experiments. High-speed video recordings and direct measurements of the internal velocity, density and temperature structure of the flows were interrogated to determine how obstacles of variable sizes perturbate the flow structure. Measurements of the spatiotemporal deposition rates across ridges and the characterization of resulting deposits were used to relate different flow environments across ridges and the time-variant flow structure to distinct facies of resulting depositional bedforms. The main results from this study can be summarized as follows:

Wall-mounted ridges induce strong changes to the vertical structure of PDCs. These changes can be associated with the passing of the PDC over three different segments of the obstacles.

At the front of the ridge, complete blocking of the PDC underflow and partial blocking of the concentrated lower region of the turbulent ash-cloud surge region cause deceleration and rapid sedimentation of these flow regions and result in mass losses of up to 90 %.

Interaction with the stoss side of the ridge causes strong compression and acceleration of the upper, non-blocked flow region. Local velocities in the accelerated flow are up to two- to three times higher than anywhere in the non-blocked PDC before the obstacle.

Behind the ridge crest, flow compression and acceleration lead to flow detachment and generation of a turbulent wake of slow and temporally reversed flow underneath the detached flow. Sedimentation inside the wake is governed by three simultaneous processes: rolling and saltation over the ridge of high-momentum coarse particles that origin from the non-detaching PDC bedload region; tractional deposition from the peripheries of eddies that form inside the wake; and sedimentation from finger-like instabilities that are generated at the interface of the wake with the detached flow. A vertically density-stratified flow is reestablished once the detached flow re-attaches downstream of the turbulent wake.

The different flow processes across these three different obstacle regions are associated with variation in deposition rates that span at least three orders of magnitude. This variation explains the strong asymmetry of deposit thickness across topographic obstacles and results in distinct vertical depositional successions that resemble those of natural PDCs.

These findings suggest that numerical hazard models that aim to simulate the propagation of PDCs across complex topography need to account for strong changes in the vertical flow structure, the effects of mass loss due to partial flow blocking, flow compressibility at the ridge stoss side and flow detachment behind the crests of obstacles. The similarity of experimental and natural PDC deposits across obstacles suggests that the spatiotemporally variable processes of particle transport and deposition can guide interpretation of natural PDC deposits.

CRediT authorship contribution statement

Lucas Corna: Writing – review & editing, Writing – original draft, Visualization, Methodology, Investigation, Formal analysis, Conceptualization. **Gert Lube:** Writing – review & editing, Supervision, Resources, Methodology, Funding acquisition, Conceptualization. **Daniel H. Uhle:** Writing – review & editing, Methodology, Formal analysis. **Ermanno Brosch:** Writing – review & editing, Visualization, Methodology. **Jim R. Jones:** Writing – review & editing, Supervision. **Michael Manga:** Writing – review & editing. **Benjamin Andrews:** Writing – review & editing.

Declaration of competing interest

The authors declare that they have no known competing financial interests or personal relationships that could have appeared to influence the work reported in this paper.

Acknowledgements

This research was partially funded by the Royal Society Te Apārangi (contracts MFP-MAU-2401, MAU-2444 and MAU-1902) and by the New Zealand Ministry of Business, Innovation and Environment (contract RTVU1704), which included a PhD scholarship for LC. MM and GL would like to acknowledge support through the KAVLI Institute of Theoretical Physics Program 'Multiphase Flows in Geophysics and the Environment' (contract no. NSF PHY-1748958). The authors would like to thank editor Dr. Lucia Capra and the two reviewers for their helpful comments on the manuscript.

Appendix A. Supplementary data

Supplementary data to this article can be found online at https://doi.org/10.1016/j.jvolgeores.2025.108469.

Data availability

Data will be made available on request.

References

Alexander, J., Morris, S., 1994. Observations on experimental, nonchannelized, high-concentration turbidity currents and variations in deposits around obstacles. J. Sediment. Res. 64 (4a), 899–909.
Andrews, B.J., Manga, M., 2011. Effects of topography on pyroclastic density current runout and formation of coignimbrites. Geology 39 (12), 12.
Andrews, B.J., Manga, M., 2012. Experimental study of turbulence, sedimentation, and coignimbrite mass partitioning in dilute pyroclastic density currents. J. Volcanol. Geotherm. Res. 225, 30–44.
Baker, C.J., 1979. The laminar horseshoe vortex. J. Fluid Mech. 95 (2), 347–367.
Belcher, S.E., Hunt, J.C.R., 1998. Turbulent flow over hills and waves. Annu. Rev. Fluid Mech. 30 (1), 507–538.
Brand, B.D., Bendaña, S., Self, S., Pollock, N., 2016. Topographic controls on pyroclastic density current dynamics: insight from 18 May 1980 deposits at Mount St. Helens, Washington (USA). J. Volcanol. Geotherm. Res. 321, 1–17.
Branney, M.J., Kokelaar, P., 2002. Pyroclastic Density Currents and the Sedimentation of Ignimbrites.
Breard, E.C.P., Lube, G., 2017. Inside pyroclastic density currents–uncovering the enigmatic flow structure and transport behaviour in large-scale experiments. Earth Planet. Sci. Lett. 458, 22–36.
Breard, E.C.P., Lube, G., Cronin, S.J., Valentine, G.A., 2015. Transport and deposition processes of the hydrothermal blast of the 6 August 2012 Te Maari Eruption, Mt. Tongariro. Bull. Volcanol. 77 (11), 100.
Breard, E.C.P., Lube, G., Jones, J.R., Dufek, J., Cronin, S.J., Valentine, G.A., Moebis, A., 2016. Coupling of turbulent and non-turbulent flow regimes within pyroclastic density currents. Nat. Geosci. 9 (10), 10.
Breard, E.C.P., Dufek, J., Lube, G., 2018. Enhanced mobility in concentrated pyroclastic density currents: an examination of a self-fluidization mechanism. Geophys. Res. Lett. 45 (2), 2.
Brosch, E., Lube, G., 2020. Spatiotemporal sediment transport and deposition processes in experimental dilute pyroclastic density currents. J. Volcanol. Geotherm. Res. 401, 106946.
Brosch, E., Lube, G., Esposti-Ongaro, T., Cerminara, M., Breard, E.C.P., Meiburg, E., 2022. Characteristics and controls of the runout behaviour of non-Boussinesq particle-Laden gravity currents–a large-scale experimental investigation of dilute pyroclastic density currents. J. Volcanol. Geotherm. Res. 107697.
Brown, R.J., Branney, M.J., 2013. Internal flow variations and diachronous sedimentation within extensive, sustained, density-stratified pyroclastic density currents flowing down gentle slopes, as revealed by the internal architectures of ignimbrites on tenerife. Bull. Volcanol. 75 (7), 7.
Burgisser, A., 2005. Physical volcanology of the 2,050 BP Caldera-forming eruption of Okmok Volcano, Alaska. Bull. Volcanol. 67 (6), 497–525.
Burgisser, A., Bergantz, G.W., Breidenthal, R.E., 2005. Addressing complexity in laboratory experiments: the scaling of dilute multiphase flows in magmatic systems. J. Volcanol. Geotherm. Res. 141 (3–4), 3–4.
Bursik, M.I., Kurbatov, A.V., Sheridan, M.F., Woods, A.W., 1998. Transport and deposition in the May 18, 1980, Mount St. Helens Blast Flow. Geology 26 (2), 155–158.

Cas, R.A.F., Wright, H.M.N., Folkes, C.B., Lesti, C., Porreca, M., Giordano, G., Viramonte, J.G., 2011. The flow dynamics of an extremely large volume pyroclastic flow, the 2.08-Ma Cerro Galán Ignimbrite, NW Argentina, and comparison with other flow types. Bull. Volcanol. 73 (10), 1583–1609.
Charbonnier, S.J., Garin, F., Rodríguez, L.A., Ayala, K., Cancel, S., Escobar-Wolf, R., Chigna, G., Chun-Quinillo, C., Gonzalez, D., Chigna, W., 2023. Unravelling the dynamics and hazards of the June 3rd, 2018, pyroclastic density currents at Fuego Volcano (Guatemala). J. Volcanol. Geotherm. Res. 436, 107791.
Choux, C.M., Druitt, T.H., 2002. Analogue study of particle segregation in pyroclastic density currents, with implications for the emplacement mechanisms of large ignimbrites. Sedimentology 49 (5), 5.
Corna, L., Jones, J., Lube, G., Brosch, E., Uhle, D., 2025. 'The Detachment of Pyroclastic Density Currents behind Topographic Obstacles: A Large-Scale Experimental Study'. Particulate Gravity Currents: Theory, Experiments, and Environmental Applications, pp. 231–247.
Cronin, S.J., Lube, G., Dayudi, D.S., Sumarti, S., Subrandiyo, S., 2013. Insights into the October–November 2010 Gunung Merapi Eruption (Central Java, Indonesia) from the stratigraphy, volume and characteristics of its pyroclastic deposits. J. Volcanol. Geotherm. Res. 261, 244–259.
Dade, W.B., Huppert, H.E., 1996. Emplacement of the Taupo ignimbrite by a dilute turbulent flow. Nature 381 (6582), 509.
Druitt, T.H., 1998. Pyroclastic density currents. Geol. Soc. Lond. Spec. Publ. 145 (1), 145–182.
Fisher, R.V., 1990. Transport and deposition of a pyroclastic surge across an area of high relief: the 18 May 1980 eruption of Mount St. Helens, Washington. Geol. Soc. Am. Bull. 102 (8), 1038–1054.
Fisher, R.V., Orsi, G., Ort, M., Heiken, G., 1993. Mobility of a large-volume pyroclastic flow—emplacement of the Campanian Ignimbrite, Italy. J. Volcanol. Geotherm. Res. 56 (3), 3.
Freundt, A., Schmincke, H.-U., 1985. Lithic-enriched segregation bodies in pyroclastic flow deposits of Laacher see volcano (East Eifel, Germany). J. Volcanol. Geotherm. Res. 25 (3–4), 3–4.
Gardner, J.E., Nazworth, C., Helper, M.A., Andrews, B.J., 2018. Inferring the nature of pyroclastic density currents from tree damage: the 18 May 1980 blast surge of Mount St. Helens, USA. Geology 46 (9), 9.
Guinn, N.K., Gardner, J.E., Helper, M.A., 2022. Dynamic pressure evolution within the 18 May 1980 Mount St. Helens pyroclastic density current: evidence from tree damage. Bull. Volcanol. 84 (4), 1–12.
Gurioli, L., Cioni, R., Sbrana, A., Zanella, E., 2002. Transport and deposition of pyroclastic density currents over an inhabited area: the deposits of the AD 79 eruption of Vesuvius at Herculaneum, Italy. Sedimentology 49 (5), 5.
Hákonardóttir, K.M., Hogg, A.J., Batey, J., Woods, A.W., 2003. Flying avalanches. Geophys. Res. Lett. 30 (23).
Hunt, J.C.R., Abell, C.J., Peterka, J.A., Woo, H., 1978. Kinematical studies of the flows around free or surface-mounted obstacles; applying topology to flow visualization. J. Fluid Mech. 86 (1), 179–200.
Komorowski, J.-C., Jenkins, S., Baxter, P.J., Picquout, A., Lavigne, F., Charbonnier, S., Gertisser, R., Preece, K., Cholik, N., Budi-Santoso, A., 2013. Paroxysmal dome explosion during the Merapi 2010 eruption: processes and facies relationships of associated high-energy pyroclastic density currents. J. Volcanol. Geotherm. Res. 261, 260–294.
Lube, G., Cronin, S.J., Platz, T., Freundt, A., Procter, J.N., Henderson, C., Sheridan, M.F., 2007. Flow and deposition of pyroclastic granular flows: a type example from the 1975 Ngauruhoe eruption, New Zealand. J. Volcanol. Geotherm. Res. 161 (3), 3.
Lube, G., Cronin, S.J., Thouret, J.-C., 2011. Kinematic characteristics of pyroclastic density currents at merapi and controls on their avulsion from natural and engineered channels. GSA Bull. 123 (5–6), 5–6.
Lube, G., Breard, E.C.P., Cronin, S.J., Procter, J.N., Brenna, M., Moebis, A., Pardo, N., Stewart, R.B., Jolly, A., Fournier, N., 2014. Dynamics of surges generated by hydrothermal blasts during the 6 August 2012 Te Maari eruption, Mt. Tongariro, New Zealand. J. Volcanol. Geotherm. Res. 286, 348–366.
Lube, G., Breard, E.C.P., Cronin, S.J., Jones, J., 2015. Synthesizing large-scale pyroclastic flows: experimental design, scaling, and first results from PELE. J. Geophys. Res. Solid Earth 120 (3), 1487–1502.
Lube, G., Breard, E.C.P., Jones, J., Fullard, L., Dufek, J., Cronin, S.J., Wang, T., 2019. Generation of air lubrication within pyroclastic density currents. Nat. Geosci. 1.
Lube, G., Breard, E.C.P., Esposti-Ongaro, T., Dufek, J., Brand, B., 2020. Multiphase flow behaviour and hazard prediction of pyroclastic density currents. Nat. Rev. Earth Environ. 1 (7), 348–365.
Mason, P.J., Morton, B.R., 1987. Trailing vortices in the wakes of surface-mounted obstacles. J. Fluid Mech. 175, 247–293.
Mason, P.J., Sykes, R.I., 1979. Separation effects in Ekman layer flow over ridges. Q. J. R. Meteorol. Soc. 105 (443), 129–146.
Moore, J.G., Rice, C.J., 1984. Chronology and character of the May 18, 1980, explosive eruptions of Mount St. Helens. Explosive Volcanism: Inception Evol. Hazards 10, 133–157.
Nasr-Azadani, M.M., Meiburg, E., 2014. Influence of seafloor topography on the depositional behavior of bi-disperse turbidity currents: a three-dimensional, depth-resolved numerical investigation. Environ. Fluid Mech. 14 (2), 2.
Oshaghi, M.R., Afshin, H., Firoozabadi, B., 2013. Experimental investigation of the effect of obstacles on the behavior of turbidity currents. Can. J. Civ. Eng. 40 (4), 343–352.
Risica, G., Rosi, M., Pistolesi, M., Speranza, F., Branney, M.J., 2022. Deposit-derived block-and-ash flows: the hazard posed by perched temporary tephra accumulations on volcanoes; 2018 Fuego disaster, Guatemala. J. Geophys. Res. Solid Earth 127 (6), 6.
Roche, O., 2012. Depositional processes and gas pore pressure in pyroclastic flows: an experimental perspective. Bull. Volcanol. 74 (8), 8.
Roche, O., Buesch, D.C., Valentine, G.A., 2016. Slow-moving and far-travelled dense pyroclastic flows during the peach spring super-eruption. Nat. Commun. 7 (1), 1.
Sulpizio, R., De Rosa, R., Donato, P., 2008. The influence of variable topography on the depositional behaviour of pyroclastic density currents: the examples of the Upper Pollara eruption (Salina Island, Southern Italy). J. Volcanol. Geotherm. Res. 175 (3), 367–385.
Sulpizio, R., Dellino, P., Doronzo, D.M., Sarocchi, D., 2014. Pyroclastic density currents: state of the art and perspectives. J. Volcanol. Geotherm. Res. 283, 36–65.
Thielicke, W., Stamhuis, E., 2014. PIVlab–towards user-friendly, affordable and accurate digital particle image velocimetry in MATLAB. J. Open Res. Softw. 2 (1).
Uhle, D.H., Lube, G., Breard, E.C.P., Meiburg, E., Dufek, J., Ardo, J., Jones, J.R., Brosch, E., Corna, L.R.P., Jenkins, S.F., 2024. Turbulent particle-gas feedback exacerbates the hazard impacts of pyroclastic density currents. Commun. Earth Environ. 5 (1), 245.
White, J.D.L., Houghton, B.F., 2006. Primary volcaniclastic rocks. Geology 34 (8), 677–680.
Wilson, C.J.N., 1985. The Taupo eruption, New Zealand. II. The Taupo ignimbrite. Philos. Trans. R. Soc. Lond. Ser. A Math. Phys. Sci. 314 (1529), 229–310.
Wilson, R.I., Friedrich, H., Stevens, C., 2018. Flow structure of unconfined turbidity currents interacting with an obstacle. Environ. Fluid Mech. 18 (6), 1571–1594.
Woods, A.W., Bursik, M.I., Kurbatov, A.V., 1998. The interaction of ash flows with ridges. Bull. Volcanol. 60 (1), 38–51.